

See discussions, stats, and author profiles for this publication at: <https://www.researchgate.net/publication/251876413>

Structural Variability in Multifunctional Metal Xylenediaminetetraphosphonate Hybrids

ARTICLE in INORGANIC CHEMISTRY · JULY 2013

Impact Factor: 4.76 · DOI: 10.1021/ic400951s · Source: PubMed

CITATIONS

12

READS

46

11 AUTHORS, INCLUDING:



Didier Villemin

Université de Caen Normandie

294 PUBLICATIONS 2,960 CITATIONS

SEE PROFILE



Gary B Hix

Nottingham Trent University

54 PUBLICATIONS 784 CITATIONS

SEE PROFILE



Konstantinos D Demadis

University of Crete

142 PUBLICATIONS 3,656 CITATIONS

SEE PROFILE



Aurelio Cabeza

University of Malaga

71 PUBLICATIONS 1,650 CITATIONS

SEE PROFILE

Structural Variability in Multifunctional Metal Xylenediaminetetraphosphonate Hybrids

Rosario M. P. Colodrero,[⊥] Giasemi K. Angeli,[#] Montse Bazaga-Garcia,[⊥] Pascual Olivera-Pastor,[⊥] Didier Villemin,[§] Enrique R. Losilla,[⊥] Estefania Q. Martos,[⊥] Gary B. Hix,[†] Miguel A. G. Aranda,^{⊥,±} Konstantinos D. Demadis,^{*,#} and Aurelio Cabeza^{*,⊥}

[⊥]Departamento de Química Inorgánica, Universidad de Málaga, Campus Teatinos s/n, 29071-Málaga, Spain

[#]Crystal Engineering Growth & Design Laboratory, Department of Chemistry, University of Crete, Voutes Campus, Crete, GR-71003, Greece

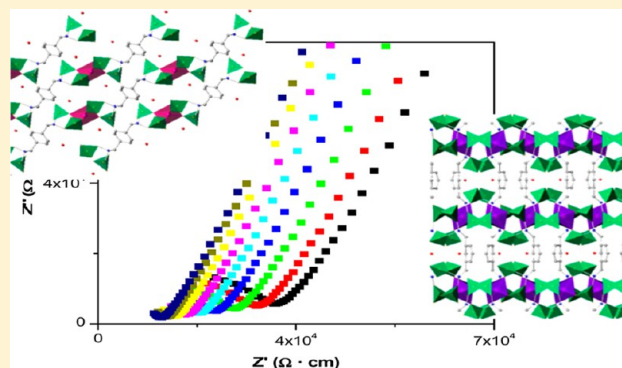
[§]Laboratoire de Chimie Moléculaire et Thioorganique, UMR CNRS 6507, INC3M, FR 3038, ENSICAEN and Université de Caen, Caen, France

[†]School of Science and Technology, Nottingham Trent University, Clifton Lane, Nottingham, NG11 8NS, United Kingdom

[±]CELLS-ALBA synchrotron, Carretera BP 1413, Km. 3.3, E-08290 Cerdanyola, Barcelona, Spain

S Supporting Information

ABSTRACT: Two new families of divalent metal hybrid derivatives from the aromatic tetraphosphonic acids 1,4- and 1,3-bis(aminomethyl)benzene-*N,N'*-bis(methylenephosphonic acid), (H₂O₃PCH₂)₂-N-CH₂C₆H₄CH₂-N(CH₂PO₃H₂)₂ (designated herein as *p*-H₈L and *m*-H₈L) have been synthesized by crystallization at room temperature and hydrothermal conditions. The crystal structures of M[(HO₃PCH₂)₂N(H)-CH₂C₆H₄CH₂N(H)(CH₂PO₃H)₂(H₂O)₂·2H₂O (M = Mg, Co, and Zn), M-(*p*-H₆L), and M[(HO₃PCH₂)₂N(H)-CH₂C₆H₄CH₂N(H)(CH₂PO₃H)₂·*n*H₂O (M = Ca, Mg, Co, and Zn and *n* = 1–1.5), M-(*m*-H₆L), were solved ab initio by synchrotron powder diffraction data using the direct methods and subsequently refined using the Rietveld method. The crystal structure of the isostructural M-(*p*-H₆L) is constituted by organic–inorganic monodimensional chains where the phosphonate moiety acts as a bidentate chelating ligand bridging two metal octahedra. M-(*m*-H₆L) compounds exhibit a 3D pillared open-framework with small 1D channels filled with water molecules. These channels are formed by the pillaring action of the organic ligand connecting adjacent layers through the phosphonate oxygens. Thermogravimetric and X-ray thermodiffraction analyses of M-(*p*-H₆L) showed that the integrity of their crystalline structures is maintained up to 470 K, without significant reduction of water content, while thermal decomposition takes place above 580 K. The utility of M-(*p*-H₆L) (M = Mg and Zn) hybrid materials in corrosion protection was investigated in acidic aqueous solutions. In addition, the impedance data indicate both families of compounds display similar proton conductivities ($\sigma \sim 9.4 \times 10^{-5} \text{ S} \cdot \text{cm}^{-1}$, at 98% RH and 297 K), although different proton transfer mechanisms are involved.



INTRODUCTION

The quest for new materials with interesting applications is the driving force for the explosion in the field of coordination polymers and metal–organic frameworks. There is substantial momentum in efforts from numerous research groups around the globe that develop in three major axes: (a) easy, reproducible, and scalable syntheses, (b) new structure types, and (c) new applications in everyday life, together with technology transfer in real industrial settings. There is a plethora of good examples in the primary and secondary literature, with several themed issues on the subject (syntheses–structures–applications)¹ of metal–organic framework (MOF) type hybrid materials, as well as monographs and books.²

The two cornerstones in the field of MOFs are secondary building units (SBU's or “bricks”) and the organic linkers. There is an impressive number of new SBU's and new (functionalized in so many ways) organic linkers/ligands, thus creating an almost infinite number of reactant combinations. We have been interested in the syntheses, structural characterization, and exploitation of various properties of phosphonate-based MOFs.³ In the area of MOFs that incorporate a phosphonate linker, developing the concept of “isorecticular” chemistry is a challenge; however, there are some examples of

Received: April 17, 2013

Published: July 24, 2013



metal phosphonates that exhibit interesting, systematically evolved structural features.^{4,5}

The structural tunability of crystalline MOFs coupled, when possible, with high chemical and thermal robustness, makes them suitable materials to correlate structure with function.^{2,5} Hence, the research focus has been set recently to the potential applications of some of these compounds, including phosphonate-based MOFs, as proton-conducting materials alternative to Nafion and related polymers.^{3a,6} These hybrid materials may offer unique proton transfer pathways in the framework of an impressive structural diversity, from 1D to 3D supramolecular networks. In this sense, tailored design of the metal linker molecules, control of the basic structural properties and dimensionality, combined with effective synthetic strategies, such as isomorphous replacements⁷ and controlled-aid impregnation of MOFs⁸ may be applied to obtain/improve proton conductivity in MOFs and polymeric materials.

On a different note, phosphonate additives, initially applied as replacements for carcinogenic chromate in metallic corrosion protection, have since then found extensive use.⁹ There is a consensus in literature reports on a *synergistic* action of dissolved M^{2+} and phosphonate ligands that has been assigned to formation of metal–phosphonate inhibiting films on the metallic surface.¹⁰ We are continuing a systematic effort to study metal–phosphonate films on metal surfaces, focusing on their accurate description at the molecular level, wherever possible. Within this framework, we studied the inhibitory effects of the aforementioned hybrids on the anticorrosion protection of carbon steel surfaces.

In addition, the metal–phosphonate hybrid materials provide new opportunities for developing multifunctional solids capable of being applied in different ways. One of such application is their use as luminescent materials.¹¹ Although the lanthanide phosphonates may be apparently the best candidates, other transition metal phosphonates have been reported to exhibit promising luminescent properties. Furthermore, fine-tuning of the characteristics of the organic linker may play an important role in determining the desired properties. Thus, in this paper, we report two families of isostructural divalent (Ca, Mg, Co, Zn) hybrid phosphonate MOFs based on the tetraphosphonate ligands 1,4- and 1,3-*bis*-(aminomethyl)benzene-*N,N'*-*bis*-(methylenephosphonic acid), $(H_2O_3PCH_2)_2-N-CH_2C_6H_4CH_2-N-(CH_2PO_3H_2)_2$, (designated herein as **p-H₈L** or **m-H₈L**, respectively). The use of these two functionalized ligands, otherwise chemically and structurally quite similar, represents a good example of how small stereochemical changes in the organic linker may dramatically affect structural features and dimensionality of the resulting solids and, hence, their final properties. With **p-H₈L**, the solids present low dimensionality (1D) within a wide range of experimental conditions. In contrast, solids containing the linker **m-H₈L** tend to acquire a 3D pillared open-framework for a wide range of metal ion sizes. In addition to synthetic aspects, structural details, and thermal behavior, we also demonstrate the multifunctional nature of these compounds by studying how the ligand characteristics affect relevant chemical properties in the solid state, such as proton conductivity, luminescence, and anticorrosive activity. Part of this work was presented in a congress.¹²

■ EXPERIMENTAL SECTION

Reagents and General Methods. All starting compounds were from commercial sources and used as received. In-house, deionized (DI) water was used for all syntheses and procedures.

Elemental analyses (CHN) were measured on a Perkin–Elmer 240 analyzer. Thermal analysis (TG-DTA) data were recorded on an SDT-Q600 analyzer from TA Instruments. The temperature was varied from RT to 773 K at a heating rate of 10 K·min^{−1}. Measurements were carried out on a sample in an open platinum crucible under a flow of air. Infrared spectra were obtained with an attenuated total reflectance (ATR) accessory (MIRacle ATR, PIKE Technologies, USA) coupled to a Fourier transform infrared (FTIR) spectrometer (FT/IR-4100, JASCO, Spain). All spectra were recorded in the 4000–600 cm^{−1} range at 4 cm^{−1} resolution, and 50 scans were accumulated.

Synthesis. The ligands 1,4-*bis*-(aminomethyl)benzene-*N,N'*-*bis*-(methanephosphonic acid) (**p-H₈L**) and 1,3-*bis*-(aminomethyl)benzene-*N,N'*-*bis*-(methanephosphonic acid) (**m-H₈L**) were synthesized according to literature procedures.¹³

Preparation of M-(p-H₈L) [M = Mg, Co, and Zn]. A quantity of the ligand **p-H₈L** (0.307 g, 0.600 mmol) is suspended in 10 mL deionized water (the ligand is not soluble in pure water). The ligand can be solubilized by addition of NaOH stock solution until the pH reaches 6.0. Then the pH of the resulting clear solution is reduced by addition of HCl stock solution until pH is 2. A quantity of ZnCl₂ (0.082 g, 0.600 mmol) is separately dissolved in 5 mL of DI water. The ZnCl₂ solution is added dropwise to the **p-H₈L** ligand solution under stirring. The pH is finally adjusted to 2.5, and the solution is left undisturbed at ambient conditions. After a couple days, a microcrystalline powder appears which is isolated by filtration, washed with DI water, and air-dried. Typical yields exceed 60%. The same procedure was followed for the Mg²⁺ and Co²⁺ analogs, by using suitable water-soluble metal salts.

Hydrothermal syntheses were also carried out following the same procedure previously described, but the reactant solutions were treated at 413 K for 3 days under autogenous pressure.

As demonstrated by crystallographic studies and elemental analyses, the three analogs reported here have the general formula $M-[(HO_3PCH_2)_2N(H)CH_2C_6H_4CH_2N(H)(CH_2PO_3H)_2(H_2O)_2] \cdot 2H_2O$ (M = Zn, Co, Mg). **Zn-(p-H₈L)**: anal calcd (%) for ZnC₁₂H₃₀O₁₆N₂P₄: 22.25% C, 4.67% H, 4.33% N. Found: 22.30% C, 4.05% H, 4.67% N. **Mg-(p-H₈L)**: anal calcd (%) for MgC₁₂H₃₀O₁₆N₂P₄: 23.84% C, 4.67% H, 4.77% N. Found: 24.20% C, 4.75% H, 4.80% N. **Co-(p-H₈L)**: anal calcd (%) for CoC₁₂H₃₀O₁₆N₂P₄: 22.47% C, 4.72% H, 4.37% N. Found: 23.33% C, 4.49% H, 4.70% N.

Preparation of M-(m-H₈L) [M = Mg, Ca, Co, and Zn]. Syntheses at room temperature were carried out by slow evaporation as previously described for **M-(p-H₈L)** compounds. The ligand **m-H₈L** (0.228–0.376 mmol) was suspended in 10 mL deionized water and solubilized at pH 2 in two steps, by consecutive addition of NaOH (up to clear solution) and HCl stock solutions (1–5 M). A 5 mL portion of a solution of the suitable metal salt [Zn(NO₃)₂·6H₂O, Mg(NO₃)₂·6H₂O, CoCl₂·6H₂O, or Ca(NO₃)₂·3H₂O] corresponding to a molar ratio M:ligand = 1:1 was then dropwise added to the ligand solution, under stirring. For all experiments, the final pH was adjusted to 2.0 and the solutions were left undisturbed at ambient conditions. After several days, the microcrystalline solids were isolated as mentioned above. Typical yields exceed 60% (except for the Mg derivative, obtained in 40% yield).

Syntheses under hydrothermal conditions were also screened by high-throughput methodology with a system previously reported.¹⁴ The aluminum autoclave block contains six Teflon-lined reaction chambers of 5 mL volume. The reaction mixture was prepared by mixing a 0.3–0.5 M aqueous solution of suitable metal salt [Mg(CH₃COOH)₂·4H₂O, Ca(NO₃)₂·3H₂O, or ZnSO₄·H₂O] with a 0.06 or 0.07 M aqueous solution of **m-H₈L** ligand. The **m-H₈L** acid was dissolved by adding dropwise an aqueous solution of (CH₃)₄NOH to the suspension of the ligand in 25 mL of DI water until a homogeneous, clear solution formed. Hydrothermal reactions of **m-H₈L** acid with Mg²⁺ and Ca²⁺ were carried out at 453 and 413 K, for two molar ratios M:**m-H₈L** (1:1 and 4:1) and several initial pH values, range between 1.6 and 4.0. For the Zn derivatives, only hydrothermal syntheses at 413 K were tested. The initial pH values were modified from 1 to 2.5 for Zn²⁺:**m-H₈L** = 1:1 and from 2 to 9 for Zn²⁺:**m-H₈L** =

Table 1. Crystallographic Data and Structure Refinements for Compounds**M[(HO₃PCH₂)₂N(H)CH₂C₆H₄CH₂N(H)(CH₂PO₃H)₂(H₂O)₂] \cdot 2H₂O (M = Mg, Co, Zn), M-(*p*-H₆L)**

reference	Zn-(<i>p</i> -H ₆ L)	Mg-(<i>p</i> -H ₆ L)	Co-(<i>p</i> -H ₆ L)
chemical formula	ZnC ₁₂ H ₃₀ O ₁₆ N ₂ P ₄	MgC ₁₂ H ₃₀ O ₁₆ N ₂ P ₄	CoC ₁₂ H ₃₀ O ₁₆ N ₂ P ₄
formula mass	647.65	606.57	641.20
crystal system	triclinic	triclinic	triclinic
space group	<i>P</i> $\bar{1}$	<i>P</i> $\bar{1}$	<i>P</i> $\bar{1}$
$\lambda/\text{\AA}$	0.2998	1.5406	1.5406
<i>a</i> /Å	6.9591(5)	6.9549(15)	6.9303(12)
<i>b</i> /Å	7.5805(4)	7.5700(10)	7.5793(8)
<i>c</i> /Å	10.6229(7)	10.6511(14)	10.6441(15)
α/deg	86.816(7)	87.071(16)	86.949(11)
β/deg	81.464(6)	81.018(10)	81.250(13)
γ/deg	73.592(5)	73.831(11)	73.514(7)
unit cell volume/Å ³	531.57(8)	531.97(19)	529.85(18)
<i>Z</i>	1	1	1
<i>V</i> _{non-H-atom} ^a /Å ³	15.19	15.19	15.14
temperature/K	293	293	293
no. independent reflections	305	455	236
data/restraints/parameters	5372/49/87	3928/46/81	3049/50/110
<i>R</i> _{WP}	0.0923	0.1505	0.0555
<i>R</i> _p	0.0678	0.1052	0.0407
<i>R</i> _F	0.0417	0.0517	0.0291
CCDC number	925414	925415	925416

^aVolume per nonhydrogen atom.**Table 2. Crystal Data and Structure Refinements for Compounds****M[(HO₃PCH₂)₂N(H)CH₂C₆H₄CH₂N(H)(CH₂PO₃H)₂] \cdot *n*H₂O (*n* = 1–1.5 and M = Mg, Ca, Co, Zn), M-(*m*-H₆L)**

reference	Ca-(<i>m</i> -H ₆ L)	Mg-(<i>m</i> -H ₆ L)	Co-(<i>m</i> -H ₆ L)	Zn-(<i>m</i> -H ₆ L)
chemical formula	CaC ₁₂ H ₂₄ O ₁₃ N ₂ P ₄	MgC ₁₂ H ₂₅ O _{13.5} N ₂ P ₄	CoC ₁₂ H ₂₄ O ₁₃ N ₂ P ₄	ZnC ₁₂ H ₂₄ O ₁₃ N ₂ P ₄
formula mass	568.30	561.53	587.15	593.61
crystal system	orthorhombic	orthorhombic	orthorhombic	orthorhombic
space group	Pmnb	Pmnb	P2 ₁ nb	Pmnb
$\lambda/\text{\AA}$	0.2998	0.2998	1.5406	1.5406
<i>a</i> /Å	22.2105(11)	22.2825(7)	22.3007(4)	22.3117(15)
<i>b</i> /Å	10.8441(4)	10.0310(4)	10.0163(4)	10.0175(5)
<i>c</i> /Å	8.6118(3)	8.5569(3)	8.6098(3)	8.6021(4)
$\alpha, \beta, \gamma/\text{deg}$	90.0	90.0	90.0	90.0
unit cell volume/Å ³	2074.18(18)	1912.61(16)	1923.17(9)	1922.64(22)
<i>Z</i>	4	4	4	4
<i>V</i> _{non-H-atom} ^a /Å ³	16.21	14.71	15.03	15.02
temperature/K	293	293	293	293
no. independent reflections	431	399	601	294
data/restraints/parameters	3803/37/68	5136/37/64	4430/79/128	3334/37/68
<i>R</i> _{WP}	0.0743	0.0771	0.0172	0.0889
<i>R</i> _p	0.0580	0.0599	0.0116	0.0700
<i>R</i> _F	0.0424	0.0347	0.0570	0.0305
CCDC number	930353	930354	933128	930355

^aVolume per non-hydrogen atom.

4:1 by adding (CH₃)₄NOH or HNO₃ aqueous solutions. A total filling volume of ~2 mL per reactor was used. The Co derivative was obtained by the same procedure as described above for the synthesis at room temperature but conducting the reaction hydrothermally at 413 K for 3 days. The reaction products were filtered off, washed with water, and dried at 323 K. Typical yields were about 55–60%.

Crystallographic studies and elemental analyses are in agreement with the formula M[(HO₃PCH₂)₂N(H)CH₂C₆H₄CH₂N(H)-(CH₂PO₃H)₂] \cdot *n*H₂O (M = Ca, Mg, Zn, Co; *n* = 1–1.5) for the reported compounds. **Ca-(*m*-H₆L)**: anal calcd (%) for CaC₁₂H₂₄O₁₃N₂P₄: 25.36% C, 4.27% H, 4.93% N. Found: 26.36% C, 4.46% H, 5.01% N. **Mg-(*m*-H₆L)**: anal calcd (%) for

MgC₁₂H₂₅O_{13.5}N₂P₄: 25.67% C, 4.49% H, 4.99% N. Found: 25.26% C, 4.12% H, 4.93% N. **Zn-(*m*-H₆L)**: anal calcd (%) for ZnC₁₂H₂₄O₁₃N₂P₄: 24.28% C, 4.07% H, 4.72% N. Found: 23.96% C, 3.43% H, 4.68% N. **Co-(*p*-H₆L)**: anal calcd (%) for CoC₁₂H₂₄O₁₃N₂P₄: 24.55% C, 4.12% H, 4.77% N. Found: 24.37% C, 4.59% H, 4.71% N.

Crystallography Study. Laboratory X-ray powder diffraction (XRPD) patterns were collected on a PANalytical X'Pert Pro diffractometer in a Bragg–Brentano reflection configuration by using a Ge(111) primary monochromator (Cu K α 1) and the X'Celerator detector. XRPD patterns were autoindexed using the DICVOL06 program¹⁵ in triclinic unit cells, for M-(*p*-H₆L), and in an

orthorhombic cell, for $M-(m-H_8L)$. For the structural determination of $Zn-(p-H_8L)$, $Mg-(m-H_8L)$, and $Ca-(m-H_8L)$, powder X-ray diffraction data were collected at the high resolution beamline ID31 of the ESRF, European Synchrotron Radiation Facility (Grenoble, France). A wavelength of 0.2998 Å was selected with a double-crystal Si (111) monochromator and calibrated with Si NIST ($a = 5.43094$ Å). The Debye–Scherrer configuration was used with the sample loaded in a rotating borosilicate glass capillary of diameter of 1.0 mm. The overall measuring time was ≈ 100 min to have very good statistics over the angular range 1.0 – 15° (in 2θ). The data from the multianalyzer Si(111) stage were normalized and summed into 0.003° step size with local software. Their crystal structures were solved following an ab initio methodology. The structure determinations were carried out by direct methods using the program Expo2009¹⁶ for $Zn-(p-H_8L)$ and $Ca-(m-H_8L)$. Partial structural models were obtained and the missing atoms were localized by difference of Fourier maps. The structures were optimized by the Rietveld method¹⁷ using the program GSAS¹⁸ and the graphic interface EXPGUI.¹⁹ The following soft constraints were imposed in order to preserve chemically reasonable geometries for the phosphonate, amine groups, methylene groups, and aromatic ring: PO_3C tetrahedron/ $P-O$ (1.53(1) Å), $P-C$ (1.80(1) Å), $O\cdots O$ (2.55(2) Å), $O\cdots C$ (2.73(2) Å), $N(CH_3)_3$ amine group/ $N-C$ (1.50(1) Å), $C\cdots C$ (2.45(2) Å) and $aryl/aromatic\ ring/C-C$ (1.40(1) Å), $C_{ring}\cdots C_{ring}$ (2.40(1) Å), $C_{ring}\cdots C_{ring}$ (2.78(1) Å). Hydrogen atoms were not included in the refinements. The final weight factors for the soft constraints were fixed between 30 and 20. Only one of the isotropic atomic displacement parameters was refined. The crystal structures of the remaining solids were obtained by Rietveld refinement using as a starting model the crystal structure of $Zn-(p-H_8L)$ and $Ca-(m-H_8L)$. Crystal structures have been deposited at CCDC, and the reference codes are also given in Table 1, for $M-(p-H_8L)$ and in Table 2 for $M-(m-H_8L)$.

On the other hand, thermogravimetric studies for the Co derivatives of both organic ligands, as representative compounds of each family, were carried out for the sample loaded in an Anton Paar HTK 1200N chamber under static air. Data were collected at 303, 323, 348, 373, 398, 423, 448, 473, 498, 523, 548 K for both compounds. All measures were done with a heating rate of $10\text{ K}\cdot\text{min}^{-1}$ and a delay time of 5 min to ensure thermal stabilization. Data acquisitions were carried out between 4° and 50° (2θ) due to the low crystallinity of the sample. A step size of 0.017° and an equivalent counting time of $230\text{ s}\cdot\text{step}^{-1}$ were used.

Proton Conductivity Study. Impedance data were collected on cylindrical pellets (~ 10 mm of diameter and ~ 1 mm of thickness) obtained by pressing ~ 0.15 g of sample at 500 MPa for 2 min between porous C electrodes (Sigracet, GDL 10 BB, no Pt). Impedance data were collected using a HP4284A impedance analyzer over the frequency range from 20 Hz to 1 MHz with an applied voltage of 1 V. All measurements were electronically controlled by the winDETA package of programs.²⁰

Electrical measurements were taken in a double-wall temperature-controlled glass chamber with a gas inlet and outlet. The temperature of the glass chamber was controlled by a Julabo F32-MA refrigerated/heating circulator from 283 to 297 K every 2 K with a heating rate of $0.4\text{ K}\cdot\text{min}^{-1}$ using EasyTEMP software. Samples were equilibrated for 40 min after each step in temperature, measured in closest vicinity to the sample. The relative humidity (RH) was obtained by a continuous flow of water-saturated nitrogen at different temperatures through the cell. The pellet was equilibrated at a given RH for 18 h to ensure a fixed water content of the sample. RH is approximately constant in the narrow measured temperature range of 14 K.

Photoluminescence. The luminescent properties of the $p-H_8L$ ligand and the $M(II)$ derivatives were recorded at room temperature as solids using a Cary Eclipse Fluorimeter, employing a solid state attachment to mount the samples. Excitation and emission spectra were recorded over appropriate wavelength ranges, using a scan rate of $100\text{ nm}\cdot\text{min}^{-1}$.

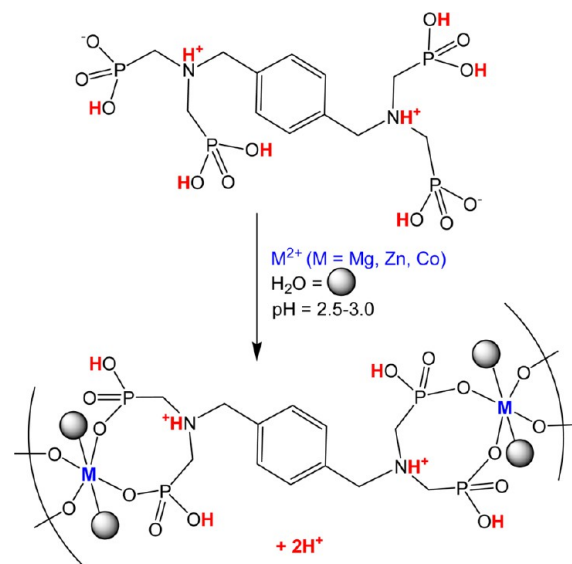
Corrosion Inhibition Study. A modified protocol is used based on NACE Standard TM0169-95 (Item No. 21200), National

Association of Corrosion Engineers, Houston TX, U.S.A.²¹ Corrosion specimens (pretreated carbon steel, grade C1010) are prepared according to the well-established protocol above. Each specimen is immersed in a control solution (no inhibitor) or in a test solution (containing either ligand $p-H_8L$ (1.0 mM) or a combination of a M^{2+} salt and $p-H_8L$ (both at (1.0 mM)) and corrosion progress is monitored by visual inspection for 7 days. Then, the specimens are removed from solution, surface samples are taken for spectroscopic studies, and corrosion products are cleaned by the standard NACE method above to determine corrosion rates from mass loss.

RESULTS AND DISCUSSION

Syntheses. The presence of highly basic N atoms on the skeleton of both ligands, $p-H_8L$ and $m-H_8L$, cause their intramolecular protonation. This is also demonstrated by the crystal structure of the “free” ligand, which shows that two phosphonic acid groups (one from each side of the aromatic ring) are monodeprotonated (and possess the form $-PO_3H^-$), whereas the remaining two are fully protonated (and possess the form $-PO_3H_2^+$) (results not shown). The N atoms are both likely protonated (NH^+) as was determined by single crystal X-ray diffraction for analog compounds.²² Protonation constants are not known for either ligands, but based on similar tetraphosphonates^{6f} at $pH \sim 2.5$ – 3.0 , both H_8L ligands should possess a “2–” overall charge with two phosphonic acid groups being fully protonated and the other two being singly deprotonated. Hence, the ligands $p-H_8L$ and $m-H_8L$ are zwitterions in their free (uncomplexed) forms; see the upper part of Scheme 1.

Scheme 1. Interaction of $p-H_8L$ with Divalent Metal Cations to Produce the 1D Hybrids



Upon interaction of $p-H_8L$ with metal ions, two further deprotonations occur on the fully protonated phosphonic acid groups. This is a well-known phenomenon for acidic ligands. Hence, the H_8L ligands now possess a total “2–” charge, with each phosphonic acid group being monodeprotonated, while the N atoms are protonated, still exhibiting a zwitterionic character.²³ It is expected that frameworks with divalent metal ions (synthesized at sufficiently low pH regions) will be neutral, due to precise charge neutralization. A generalized reaction can be envisioned (proton content on the $p-H_8L$ ligand, as example, is also shown color-coded), Scheme 1.

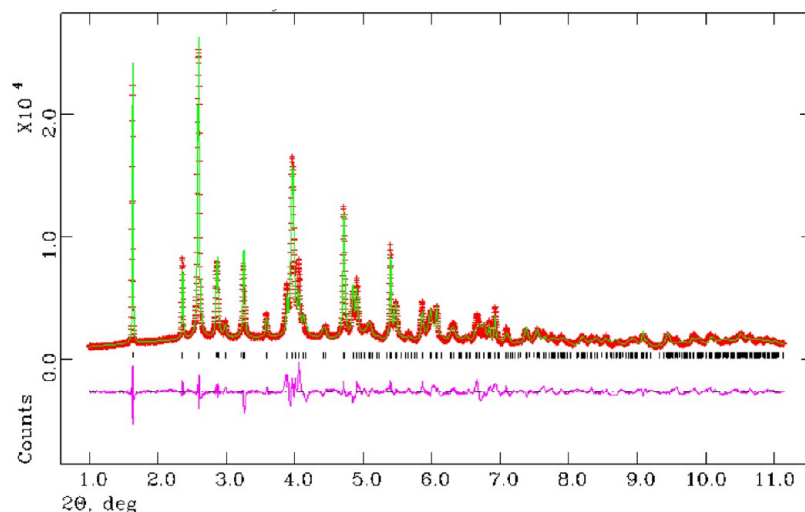


Figure 1. Final observed (crosses), calculated (solid line), and difference plots for the Rietveld refinement of synchrotron XRPD data for **Zn-(p-H₆L)**. The vertical bars highlight the positions of the allowed diffraction peaks.

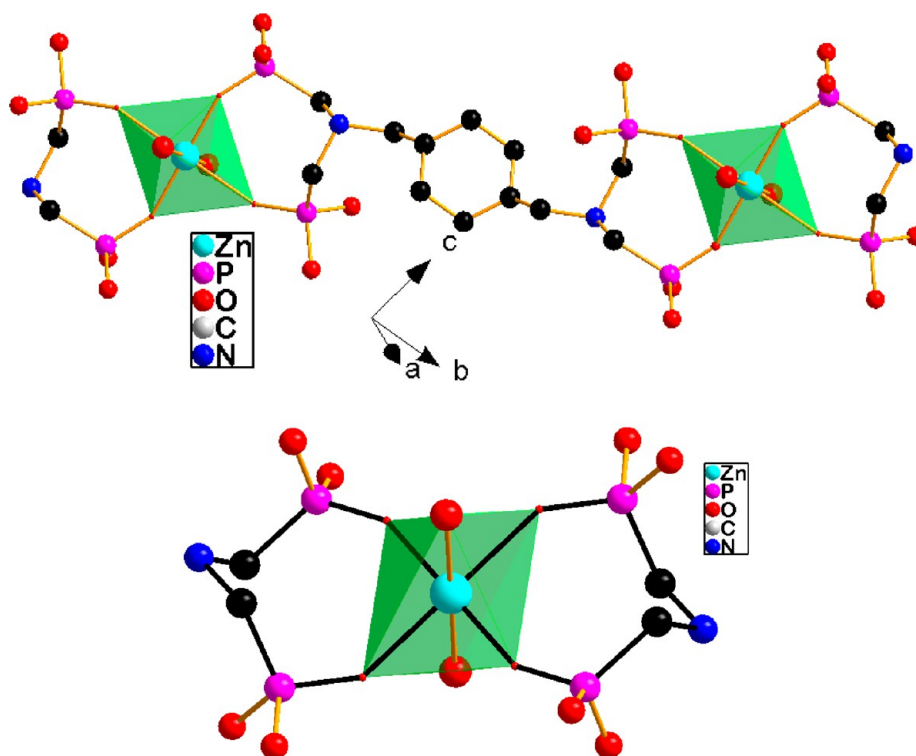


Figure 2. (upper) Basic structural "dimeric" unit for **Zn-(p-H₆L)** (the structure is the same for the Mg and Co derivatives). (lower) Zn coordination environment. Bonds in the 8-membered rings are highlighted in black. The waters of crystallization are omitted for clarity.

Under this principle of electroneutrality, **M-(p-H₆L)** (**M** = Mg, Zn, and Co) and **M-(m-H₆L)** (**M** = Ca, Mg, and Co) were isolated as microcrystalline solids by slow crystallization at room temperature, as for other divalent metal tetraphosphonates.^{4h,6f} However, no crystalline material could be prepared by the reaction of **m-H₈L** with the **Zn²⁺** solution at pH 2. Lower pH values led to the precipitation of the ligand alone.

The high effectiveness observed for the reaction between **p-H₈L** ligand with divalent metal salts at room temperature seems in contrast to the results obtained under hydrothermal conditions. Thus, only **Co-(p-H₆L)** was obtained hydrothermally as a highly crystalline solid, as confirmed by its X-ray powder diffraction pattern (see the SI, Figure S1). An

amorphous solid was isolated for Zn and no product was isolated for Mg under similar synthetic conditions.

The high-throughput screening of the system **Zn²⁺/m-H₈L** did not reveal any solid at 453 or 413 K by hydrothermal reaction for 1:1 and 4:1 **Zn:m-H₈L** molar ratios in the studied pH range, 2.0–9.0. A single crystalline solid, **Zn-(m-H₈L)**, was isolated at 413 K for a molar ratio 1:1 and pH = 1. Similar results were obtained for the calcium derivative. Thus, amorphous solids were obtained at 413 K < *T* < 453 K, for both 1:1 and 4:1 metal/ligand molar ratios, in the whole pH range. **Ca-(m-H₈L)** could be obtained as crystalline material using a **Ca:m-H₈L** molar ratio 1:1, at pH ~ 1.6, and *T* ≤ 413 K. **Mg-(m-H₈L)**, could be prepared with high crystallinity at

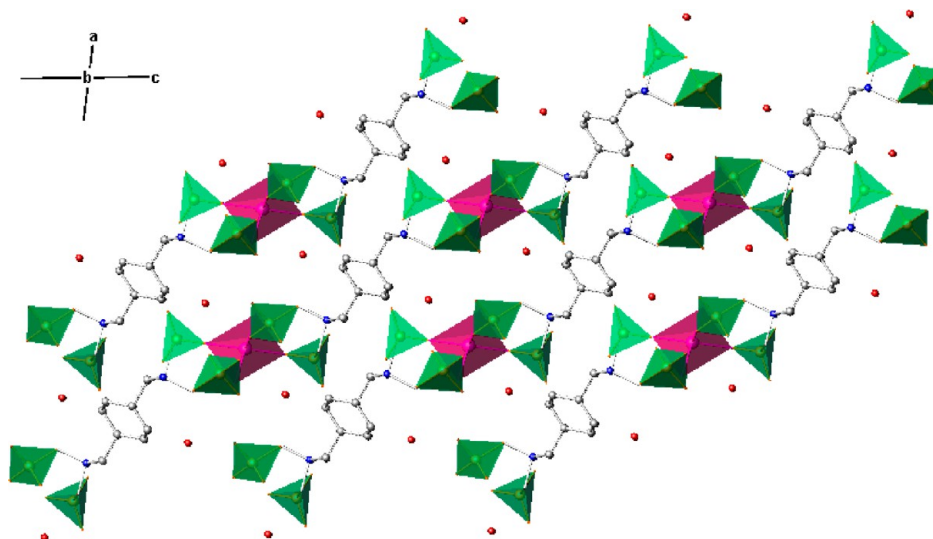


Figure 3. Packing of the hybrid chains in the crystal structure of $M[(\text{HO}_3\text{PCH}_2)_2\text{N}(\text{H})\text{CH}_2\text{C}_6\text{H}_4\text{CH}_2\text{N}(\text{H})(\text{CH}_2\text{PO}_3\text{H})_2(\text{H}_2\text{O})_2] \cdot 2\text{H}_2\text{O}$ ($M = \text{Mg}, \text{Co}, \text{Zn}$). Color codes: O_3PC tetrahedra, green; MO_6 octahedra, purple.

variable molar ratio (1:1 or 4:1), temperature (453 or 413 K), and pH 2.0–3.4. Higher pH values gave amorphous solids. With this ligand, the compounds obtained hydrothermally exhibit higher crystallinity than those prepared by crystallization at room temperature (Supporting Information Figure S2). In general, yields between 50 and 60% were obtained.

Crystal Structures. $M[(\text{HO}_3\text{PCH}_2)_2\text{N}(\text{H})\text{CH}_2\text{C}_6\text{H}_4\text{CH}_2\text{N}(\text{H})(\text{CH}_2\text{PO}_3\text{H})_2(\text{H}_2\text{O})_2] \cdot 2\text{H}_2\text{O}$. All $M-(p\text{-H}_6\text{L})$ ($M = \text{Mg}, \text{Co}, \text{Zn}$) compounds crystallize in the triclinic system and are isostructural. The crystal structure of the Zn derivative was solved ab initio from synchrotron powder diffraction data and was used as a starting model for the Rietveld refinement of the remaining two compounds. The final Rietveld plot for $\text{Zn}-(p\text{-H}_6\text{L})$ is given in the Figure 1 and those corresponding to Mg and Co derivatives are given as Supporting Information (Figures S3 and S4, respectively). Relevant crystallographic data are presented in Table 1.

The asymmetric part of the unit cell contains one M^{2+} ion, located in a special position, half a unit of the $p\text{-H}_6\text{L}^{2-}$ ligand, possessing an inversion center in the aromatic ring, and two crystallographically independent water molecules. The ligand molecule is assumed to adopt a zwitterionic form as indicated below.²³ Although hydrogens could not be located in the present crystallographic analyses, several superimposed bands of medium intensity, appearing at 2600–2200 cm^{-1} in the FT-IR spectra, might be attributed to $\text{R}_3\text{N}-\text{H}^+$ vibration modes.²⁴

All three $\text{Zn}-(p\text{-H}_6\text{L})$, $\text{Mg}-(p\text{-H}_6\text{L})$, and $\text{Co}-(p\text{-H}_6\text{L})$ show a monodimensional network built from organic–inorganic chains linked to each other through H-bonds. The basic “dimeric” building block of the chains is given in Figure 2. The chains are composed of ligand molecules with each bisphosphonate end being linked to a M^{2+} ion in a bidentate fashion. M^{2+} distorted octahedral are formed by four equatorial oxygens from four phosphonate groups of two neighboring $p\text{-H}_6\text{L}^{2-}$ molecules and two additional water molecules (Ow1) in apical positions. A second crystallographically independent water molecule Ow2 is only interacting by hydrogen bond with the phosphonate groups, connecting adjacent chains. $\text{M}-\text{O}$ bond distances and angles are shown in Supporting Information Table S1.

The metal polyhedra are bridged by the $p\text{-H}_6\text{L}^{2-}$ moiety which acts as a chelating ligand through the oxygens O1 and O4 of two crystallographically independent phosphonates forming 8-membered rings. This way of coordination results in infinite chains running parallel along the c -axis (Figure 3). Uncoordinated oxygen atoms from the phosphonate groups point outside of the chains and they are linked to each other and metal-bound water molecules by strong H-bonds. The 3D structure is stabilized by $\text{O}-\text{H}\cdots\text{O}$ hydrogen bonding and possibly weak interactions $\text{N}-\text{H}\cdots\text{O}$. The contribution of stabilizing $\pi-\pi$ interactions between phenyl rings may be neglected because they are too far apart from each other²² (see Supporting Information Figure S5 and Tables S2–S4).

As shown for $\text{Co}-(p\text{-H}_6\text{L})$, this structure is preserved even when the synthesis is carried out under hydrothermal conditions at 413 K. In contrast to this finding, $\text{Ca}-(p\text{-H}_6\text{L})$, obtained hydrothermally at 423 K, exhibits a 3D pillared framework, with xylenediamine groups connecting layers composed of alternating CaO_6 - and PO_3C -polyhedra.²² The structural variability, observed in these two compounds, associated to changes in connectivity to the metal ion, may be attributed either to a variation in preference of coordination according to the metal ionic radii and/or slight changes in the hydrothermal synthesis of the products, with higher temperatures ($T \geq 423$ K) of reaction favoring higher connectivities. The importance of reaction temperature in determining the metal/tetraphosphonate ligand connectivity is also supported by the fact that the compound $\text{Mn}[(\text{HO}_3\text{PCH}_2)_2\text{N}(\text{H})(\text{CH}_2)_4(\text{H})\text{N}(\text{CH}_2\text{PO}_3)_2]$ hydrothermally synthesized at 423 K also exhibits a 3D pillared framework.^{23b} By slightly lowering the reaction temperature at 413 K, as is the case here, the ligand seems to coordinate only to the metal ions possessing ionic radii in the vicinity of 0.7 Å (Mg^{2+} 0.72 Å, Zn^{2+} 0.74 Å, and $\text{Co}_{\text{LS}}^{2+}$ 0.65 Å or $\text{Co}_{\text{HS}}^{2+}$ 0.74 Å) in a single bidentate fashion. This coordination mode leaves room for two water molecules to enter the metal coordination sphere in a trans configuration, thus resulting in a 1D solid.

There are only a few examples of monodimensional polymeric divalent metal tetraphosphonates. One family of 1D solids, $\text{M}^{\text{II}}\text{-HDTMP}$, [$(\text{M} = \text{Sr}^{2+},^{25a} \text{Ba}^{2+},^{25a,b} \text{Cu}^{2+},^{25a} \text{HDTMP} = \text{hexamethylenediamine-tetrakis(methylenephos-$

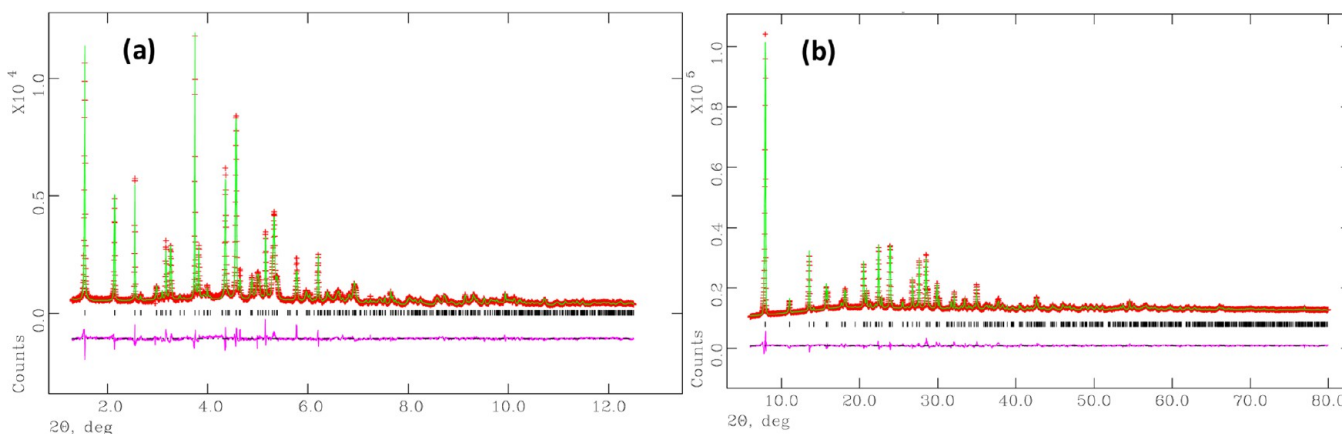


Figure 4. Final observed (crosses), calculated (solid line), and difference plots for the Rietveld refinements of (a) $\text{Ca}-(m\text{-H}_6\text{L})$, synchrotron XRPD data at 0.2998 Å and (b) $\text{Co}-(m\text{-H}_6\text{L})$, laboratory XRPD. The vertical bars highlight the positions of the allowed diffraction peaks.

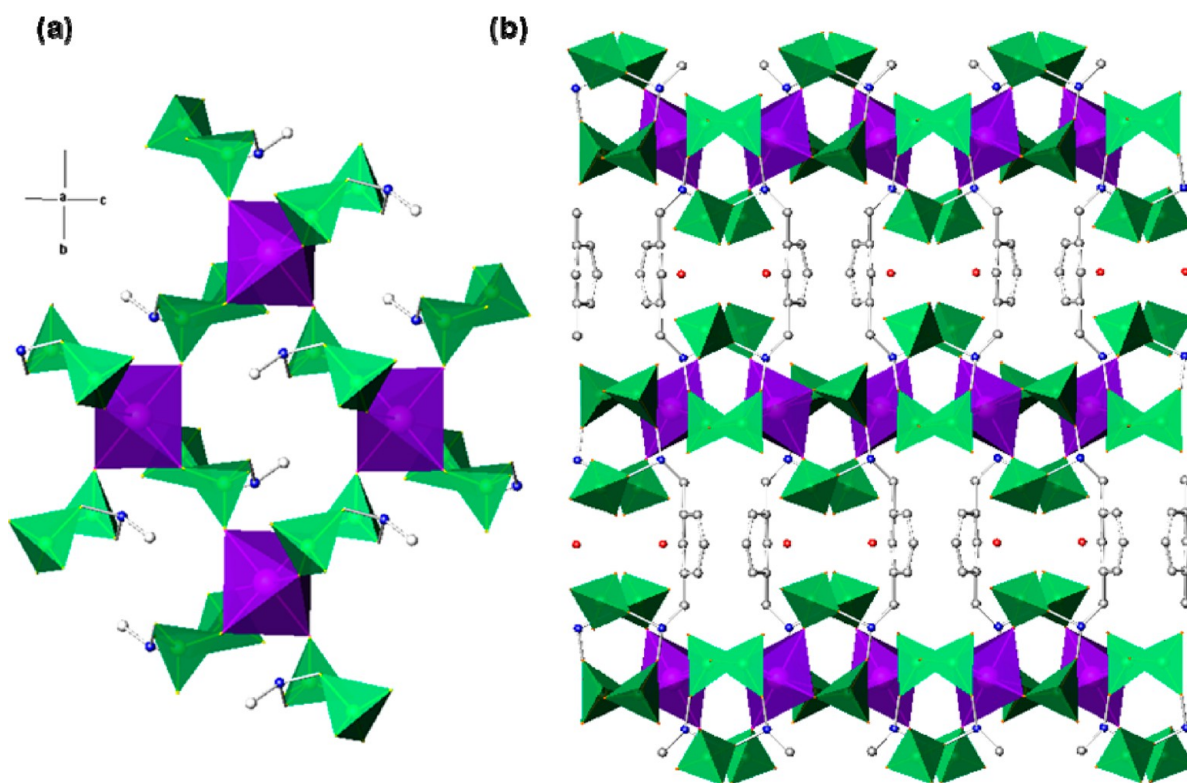


Figure 5. (a) Detail of the connectivity in the inorganic layer for $\text{M}-(m\text{-H}_6\text{L})$ ($\text{M} = \text{Ca}, \text{Mg}, \text{Co}, \text{and Zn}$). (b) 3D open-framework, viewed along the $[010]$.

phonic acid), $(\text{H}_2\text{O}_3\text{PCH}_2)_2\text{N}(\text{CH}_2)_6\text{N}(\text{CH}_2\text{PO}_3\text{H}_2)_2$, show a one-dimensional hybrid chain structure, where only one phosphonate group of each aminomethylenephosphonic motif is coordinated to the metal center by one oxygen atom. The other uncoordinated phosphonate group interacts with neighboring $-\text{PO}_3\text{H}^-$ moieties and H_2O molecules by hydrogen bonds. The other series, $\text{M}^{\text{II}}\text{-EDTMP}^{27}$ ($\text{M} = \text{Ca}, \text{Sr}$) are monodimensional solids with the tetraphosphonate EDTMP (ethylenediamine-*tetrakis*(methylenephosphonic acid), $(\text{H}_2\text{O}_3\text{PCH}_2)_2\text{N}(\text{CH}_2)_2\text{N}(\text{CH}_2\text{PO}_3\text{H}_2)_2$), again formed by the double chelating-bridging function of the tetraphosphonate ligand.

$\text{M}[(\text{HO}_3\text{PCH}_2)_2\text{N}(\text{H})\text{CH}_2\text{C}_6\text{H}_4\text{CH}_2\text{N}(\text{H})(\text{CH}_2\text{PO}_3\text{H}_2)_2]\cdot n\text{H}_2\text{O}$ ($n = 1\text{--}1.5$). $\text{M}-(m\text{-H}_6\text{L})$ ($\text{M} = \text{Ca}, \text{Mg}, \text{Co}, \text{Zn}$) can be obtained as polycrystalline solids by crystallization at room

temperature or hydrothermally. Their X-ray patterns were indexed in similar orthorhombic unit cells. The extinction conditions were consistent with the space groups $Pmnb$ or $P2_1nb$. So, initially, the centrosymmetric space group $Pmnb$ was selected for ab initio structural solution by direct methods using the synchrotron powder diffraction data collected for $\text{Ca}-(m\text{-H}_6\text{L})$. Its crystal structure could be fully completed and refined in the centrosymmetric space group and the final structure was used as a starting model for the Rietveld refinements of the remaining compounds. These refinements converged for the remaining solids except for cobalt derivative. A difference Fourier map for this solid revealed a slight different orientation of the aromatic ring, with the carbon atoms C5 and C7 of the aromatic ring out of the special position $(0.75, y, z)$ that they are occupying in the centrosymmetric group. Therefore, the

noncentrosymmetric space group $P2_1nb$ was adopted for the final Rietveld refinement for $\text{Co}-(m\text{-H}_6\text{L})$. Figure 4 shows the final Rietveld plots for $\text{Ca}-(m\text{-H}_6\text{L})$ and $\text{Co}-(m\text{-H}_6\text{L})$. Those other Rietveld plots corresponding to the Mg and Zn derivatives are given as Supporting Information (Figures S6 and S7, respectively). Relevant crystallographic data for $\text{M}-(m\text{-H}_6\text{L})$ ($\text{M} = \text{Ca}, \text{Mg}, \text{Co}, \text{Zn}$) are presented in Table 2.

All $\text{M}-(m\text{-H}_6\text{L})$ show a 3D pillared open-framework where the inorganic layer exhibits the same mixed bidentate/monodentate metal/ligand connectivity as already described for $\text{Ca}-(p\text{-H}_6\text{L})$.²² The asymmetric part of the unit cell contains one M^{2+} ion, located in a special position, a half unit of the $m\text{-H}_6\text{L}^{2-}$ ligand, for $\text{M}-(m\text{-H}_6\text{L})$ solids ($\text{M} = \text{Ca}, \text{Mg}, \text{Zn}$), and one crystallographically independent lattice water in special position. For $\text{Co}-(m\text{-H}_6\text{L})$, the asymmetric part contains a full unit of the $m\text{-H}_6\text{L}^{2-}$ ligand, besides the metal atom and the lattice water. Compound $\text{Mg}-(m\text{-H}_6\text{L})$ crystallizes with an additional half water molecule per formula, but it could not be found by Fourier differences. In general, the inorganic layers are built from M^{2+} distorted octahedra (see Supporting Information Table S5 and S6). As for $\text{M}-(p\text{-H}_6\text{L})$ compounds, four equatorial oxygens come from four phosphonate groups of two $m\text{-H}_6\text{L}^{2-}$ molecules; however the oxygen atoms in axial position are occupied by two other phosphonate groups instead of water molecules. So, in this case, the tetraphosphonate units act as chelating as well as a monodentate ligands forming 8-membered ring nets composed of alternating MO_6 -octahedra and PO_3C -polyhedra (Figure 5a).²² In this case, neighboring layers, are connected along the a -axis by the xylenediamine groups. However, the presence of the diamine-tetraphosphonates groups in meta-position relative to the aromatic ring favors the presence of 1D channels running parallel to the b -axis within the interlayer region (Figure 5b). Tilting and alternating arrangement of the aromatic rings impedes, however, the existence of such channels in the framework of $\text{Ca}-(p\text{-H}_6\text{L})$. The lattice water is situated close to the center of the channels interacting by H-bond with an oxygen atom of the phosphonate group that acts as monodentate ligand ($\text{O}\cdots\text{O}$ interacting distance between 2.63 and 2.90 Å). The second non-coordinating oxygen of this phosphonate group also points inward the channels, and it is strongly interacting by H-bond (~ 2.45 Å) with an equivalent oxygen atom of the phosphonate group of the adjacent layer.

It should be noted that this framework is adopted by a number of divalent ions, within a wide range of sizes, and even though the reactions were conducted at room temperature. This coordination mode is not only interesting by the high dimensionality (3D) of the resulting solids, but also because the absence of water directly coordinated to the metal centers, which in turn may reinforce properties such as luminescence. The absence of metal bound water is also a noticeable characteristic in other tetraphosphonate ligand-based 3D pillared frameworks^{6e,f} presenting a remarkable high proton conductivity. The latter compounds, however, show distinctive metal/ligand coordination, with metal center being now connected to six oxygens of six different phosphonate groups.

The connectivity showed by the $p\text{-H}_6\text{L}^{2-}$ and $m\text{-H}_6\text{L}^{2-}$ ligands with many divalent metal ions contrasts with that corresponding to Cu^{2+} derivatives. For both derivatives, the tetraphosphonate moiety acts as *endo*-tridentate ligand,²⁶ where the N atom also participates in chelating the metal centers. Besides, the different conformation induced by the xylene groups with the substituent in para or meta determine the

network of the resulting compounds. Thus, although both compounds show 2D frameworks, $\text{Cu}-(p\text{-H}_6\text{L})$ is built by anionic organic–inorganic layers which charge is compensated by additional $\text{Cu}(\text{H}_2\text{O})_6^{2+}$ ions. However, $\text{Cu}-(m\text{-H}_6\text{L})$ shows neutral organic–inorganic layers where the presence of the m -xylene groups induces the formation of hydrophilic hemi-cavities, occupied by water molecules, between adjacent layers.²⁶

Thermal Behavior and IR Spectroscopy. Thermal stabilities of $\text{M}-(p\text{-H}_6\text{L})$ and $\text{M}-(m\text{-H}_6\text{L})$ solids were studied by TG-DTA analysis and X-ray thermodiffraction. Thermogravimetric analyses for $\text{M}-(p\text{-H}_6\text{L})$ are displayed in Figure 6a.

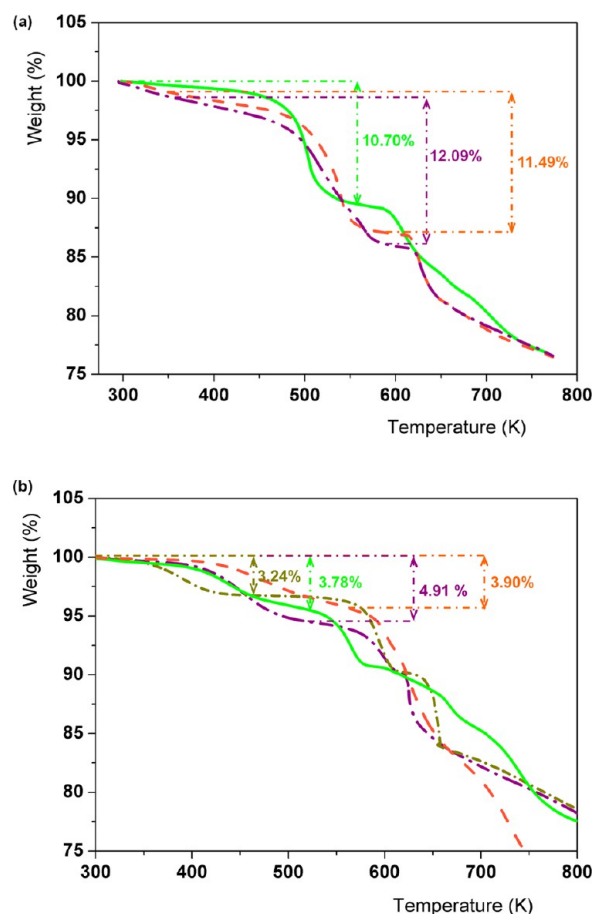


Figure 6. TGA curves for (a) $\text{M}-(p\text{-H}_6\text{L})$ and (b) $\text{M}-(m\text{-H}_6\text{L})$ solids [$\text{M} = \text{Zn}$ (green), $\text{M} = \text{Co}$ (orange), $\text{M} = \text{Mg}$ (purple), and $\text{M} = \text{Ca}$, (dark green)].

$\text{Zn}-(p\text{-H}_6\text{L})$ is stable up to 423 K. Water was completely removed between 423 and 553 K (10.7%, calculated 11.1%), but a clear distinction between bound and lattice water molecules was not apparent, as they are removed in one step. Thermal decomposition of the hybrid compound takes place above 583 K. $\text{Mg}-(p\text{-H}_6\text{L})$ and $\text{Co}-(p\text{-H}_6\text{L})$ solids show similar thermal behavior, demonstrated by a gradual weight loss from room temperature up to 583 K. The overall associated weight loss of 13.10% and 12.30%, respectively, corresponds to a water content slightly higher than four molecules per formula (11.87% and 11.20%, respectively), attributed to the loss of some physisorbed water at low temperature. Thermal decomposition of the phosphonate ligand starts above 600 K.

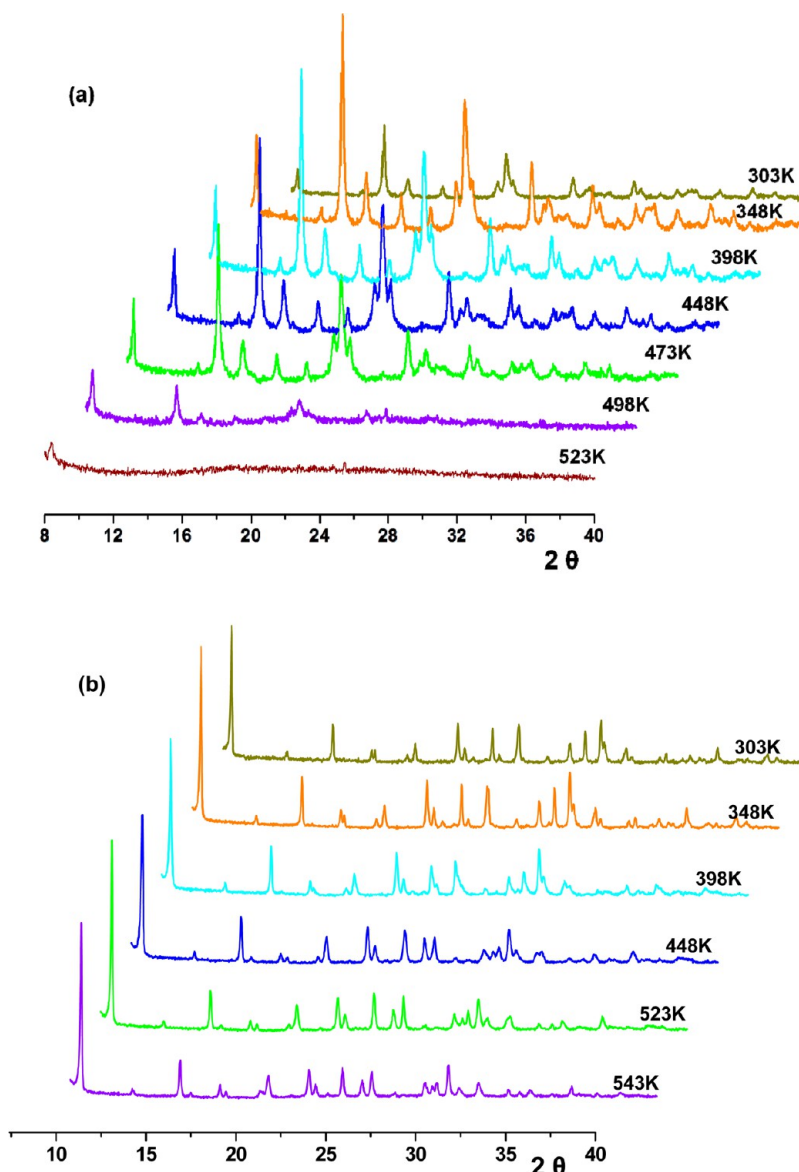


Figure 7. Thermodiffractometric studies for (a) $\text{Co}-(p\text{-H}_6\text{L})$ and (b) $\text{Co}-(m\text{-H}_6\text{L})$ in the 303–543 K temperature range.

The TGA curves for $\text{M}-(m\text{-H}_6\text{L})$, Figure 6b, show two well-defined weight losses corresponding to the removal of the lattice water (endothermic peak in DTA curves) and the combustion of the organic moiety (exothermic peaks in DTA curves). For $\text{Ca}-(m\text{-H}_6\text{L})$, the water molecule is eliminated between 340 and 423 K. The overall associated weight loss of 3.1% is in agreement with that calculated (3.0%) for one water molecule. The resulting anhydrous phase is stable up to 570 K, above which the combustion of the ligand starts. Zn and Co derivatives behave similarly, with associated weight losses of 3.8% and 3.9% (calculated, 3.0% and 3.1%), respectively. For both compounds, the mass loss takes place sequentially between 360–493 K [$\text{Zn}-(m\text{-H}_6\text{L})$] and 360–550 K [$\text{Co}-(m\text{-H}_6\text{L})$]. A slightly higher range of temperature was observed for the dehydration of $\text{Mg}-(m\text{-H}_6\text{L})$ (405–570 K). The measured water loss, 4.9%, agrees well with the 4.8% calculated for 1.5 water molecules. The anhydrous phases formed start to decompose almost immediately exhibiting different patterns, that of the cobalt derivative showing the fastest decomposition.

Thermodiffractometric analyses were carried out to precisely monitor possible structural changes upon thermal treatments for two samples as representative members of each series: $\text{Co}-(p\text{-H}_6\text{L})$, Figure 7a, and $\text{Co}-(m\text{-H}_6\text{L})$, Figure 7b. The Rietveld refinement for $\text{Co}-(p\text{-H}_6\text{L})$ heated in situ at 473 K (Rietveld fit, Supporting Information Figure S8) shows a slight increase in the unit cell volume, from 529.8(1) to 533.7(3) Å³, as a consequence of a small thermal expansion of the cell. It should be noted that the disagreement factors increase more than 2% when the lattice water is not taken into account in the Rietveld refinement. This confirms that only a small fraction of water has been removed in agreement with the thermal analysis (~2.7%). Complete removal of water at higher temperature causes amorphization of the solids, although decomposition of the organic portion does not take place below 580 K. During the thermal treatment and up to 473 K, the crystal structure is not significantly modified. Only small structural changes are noted, the main feature being a rotation of the phosphonate group P2 causing an additional distortion and tilting of the CoO_6 octahedra (Supporting Information Figure S9 and Table S7).

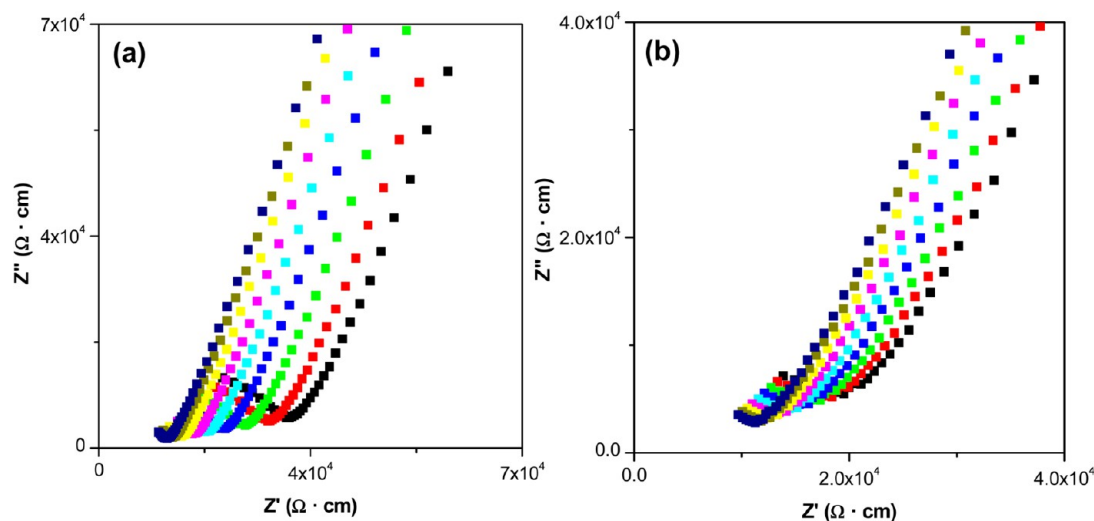


Figure 8. Plot of the complex impedance plane for (a) $\text{Mg}-(p\text{-H}_6\text{L})$ and (b) $\text{Zn}-(m\text{-H}_6\text{L})$ at 98% RH and nine temperatures: 283 (black), 285 (red), 286 (green), 288 (blue), 290 (cyan), 292 (magenta), 293 (yellow), 295 (dark yellow) and 297 K (navy).

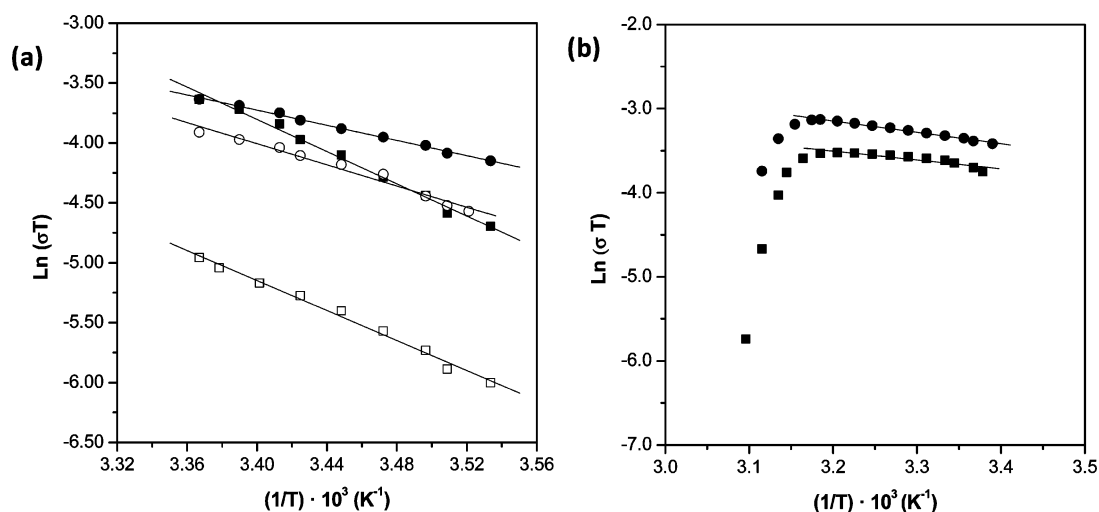


Figure 9. (a) Arrhenius plots vs T^{-1} for $\text{Mg}-(p\text{-H}_6\text{L})$ (square symbols) and $\text{Zn}-(m\text{-H}_6\text{L})$ (circle symbols) at two relative humidities 69% (open) and 98% (solid). (b) Arrhenius plots vs T^{-1} for $\text{Mg}-(p\text{-H}_6\text{L})$ (square symbols) and $\text{Zn}-(m\text{-H}_6\text{L})$ (circle symbols) in the temperature range 296 at 314 K (samples initially exposed to 98% RH).

Thus, the angle in the equatorial plane O1-Co-O4 varies from $89.5(8)^\circ$ to $81.8(8)^\circ$ upon heating at 473 K. $\text{Co}-(m\text{-H}_6\text{L})$ maintains its crystalline integrity upon thermal dehydration (Figure 7b), with only minor changes in the unit cell parameters (small contraction of a and b parameters) and a slightly higher distortion of the metal coordination sphere (see Supporting Information Figure S10). The Rietveld plot corresponding to the structural refinement of the sample $\text{Co}-(m\text{-H}_6\text{L})$ heated at 543 K is given in Supporting Information Figure S11. The refined unit cell parameters for this sample were $a = 22.083(2)$ Å, $b = 9.8540(8)$ Å, $c = 8.7553(9)$ Å, and $V = 1905.2(4)$ Å³. Rehydration was not observed when the sample was placed under a controlled humid atmosphere of a saturated NaCl solution at room temperature, for several days.

The IR spectra (Supporting Information Figures S12 and S13) of both families of hybrids tetraphosphonates show similar spectroscopic features and only small differences in the widths and intensities of the bands are observed. For $\text{M}-(p\text{-H}_6\text{L})$, the different nature of the water molecules found previously by X-

ray diffraction analysis may be also appreciated. So, two different bands in the O–H stretching region are distinguished: (1) a small and sharp band at ~ 3605 cm^{−1}, corresponding to coordinated water, that is absent for $\text{M}-(m\text{-H}_6\text{L})$ solids; and (2) a broader band centered at 3200 cm^{−1} typical of water molecules interacting strongly through H-bonds. So, the absence of the band at 3600 cm^{−1} for $\text{M}-(p\text{-H}_6\text{L})$ confirms the lability of the water for these latter compounds. The bending H–O–H vibration of the water is located at 1630 cm^{−1}, as a broad band. Two other bands observed at 2861 and 2333 cm^{−1} are likely due to $\nu(\text{P-OH})$ and the overtone $2\delta(\text{P-O-H})$, respectively. The multiple bands associated with the phosphonate groups, in the 900–1200 cm^{−1} region,²⁸ as well as the aromatic and aliphatic C–H stretching vibrations are found in positions similar to other metal phosphonates.^{25,27,28}

Proton Conductivity Results. Ionic conduction in solid state materials²⁹ occurs intrinsically through the material or via some carrier mediated pathway (e.g., H_2O , H_3O^+ , OH^- , etc.). Preliminary proton conductivity studies have been conducted for samples $\text{Mg}-(p\text{-H}_6\text{L})$ and $\text{Zn}-(m\text{-H}_6\text{L})$. Upon humid-

ification for more than 18 h, both samples exhibited stable conductivities values (Supporting Information Figure S14) which confirms the role of water as proton carrier and grain boundary remover. Impedance spectra for **Mg**–(*p*-H₆L) and **Zn**–(*m*-H₆L) at two different relative humidities (RH), 69 and 98%, and a temperature range from 283 to 297 K are shown in the SI (Figures S15 and S16) and Figure 8, respectively.

When **Mg**–(*p*-H₆L) and **Zn**–(*m*-H₆L) are exposed to the highest RH value of 98%, spikes are observed which have associated capacitances of $\sim 1 \mu\text{F}$. The spikes are inclined to the Z-axis by $\sim 70^\circ$, and this indicates a partial-blocking electrode response that allows limited diffusion; therefore, the conducting species must be ionic, i.e. H^+ ions. The total pellet resistances, R_T , were obtained from the intercept of the spikes and/or the arcs (low frequency end) on the Z-axis. At 98% RH and $T = 297 \text{ K}$, σ are close to $9.4 \times 10^{-5} \text{ S}\cdot\text{cm}^{-1}$ for both compounds. This value is intermediate between those characteristic of some phosphonate-based MOF materials ($\sigma \sim 3.5\text{--}5 \times 10^{-5} \text{ S}\cdot\text{cm}^{-1}$, at 298 K and 95–98% RH)^{29,30} and those reported for other metal tetraphosphonates ($1.6\text{--}8 \times 10^{-3} \text{ S}\cdot\text{cm}^{-1}$),^{6e,f} as well as some MOF materials exhibiting proton conductivities near to $10^{-2} \text{ S}\cdot\text{cm}^{-1}$.^{6h,7,8} As expected for water-mediated proton conductors, decreasing RH results in lower conductivities; see Supporting Information Figure S15 and S16.

The overall pellet conductivities for **Mg**–(*p*-H₆L) and **Zn**–(*m*-H₆L), in traditional Arrhenius format, are given in Figure 9a for two RH values. The derived activation energies for **Mg**–(*p*-H₆L) were $\sim 0.50 \text{ eV}$, for both RH values, and 0.25 and 0.35 eV for 98% and 69% RH, for **Zn**–(*m*-H₆L). The latter material exhibits activation energies within the range typically attributed to a Grotthuss transfer mechanism *via* water molecules, 0.1–0.4 eV.³¹

These values are consistent with those found for other 3D pillared metal phosphonates containing monodimensional channels filled with uncoordinated water which participates in H-bond networks with the POH groups pointing inward the channels.^{6e,f} However, for the monodimensional solid the activation energies are slightly high to be attributed to a Grotthuss transfer mechanism and indicate some other processes such as direct diffusion of additional protons with water molecules (vehicle mechanism). The vehicle mechanism implies the diffusion of hydrated protons or proton-containing groups, e.g. H_3O^+ , as a whole in a medium of low viscosity and high diffusion. This proton-transport has been reported in many acid solid hydrates, perovskites, zeolites, etc.^{32–34} The 1D compound ferrous oxalate dehydrate, which possesses a remarkably high conductivity at room temperature ($1.3 \times 10^{-3} \text{ S}\cdot\text{cm}^{-1}$), also presents a metal coordination sphere with two axial positions being occupied by water molecules.^{6a} However, differently from **M**–(*p*-H₆L), the arrangement of the coordinated water molecules in ferrous oxalate allows formation of strong hydrogen bonds with the framework oxalate oxygen atoms. In addition, the metal centers are well separated by a long organic linker. In this case, the more labile lattice water establishing hydrogen bond networks with the free POH groups seems to be responsible for the measured conductivities.

In these materials, the proton conductivity is thermally activated. Starting with samples pellets at 297 K and 98% RH (Figure 9), the conductivity slightly increases with the temperature up to 314 K (1.39×10^{-4} and $9.75 \times 10^{-5} \text{ S}\cdot\text{cm}^{-1}$ for **Zn**–(*m*-H₆L) and **Mg**–(*p*-H₆L) respectively), above which it drops dramatically. This behavior, observed for other MOF-based proton conductors, may be attributed to

a diminution of the conductivity by drastically decreasing the number of proton carriers.^{6a}

Photoluminescence Results. The *p*-H₆L phosphonic acid precursor and the derivatives derived from Mg and Zn exhibit a photoluminescent response (Figure 10), while the Co based

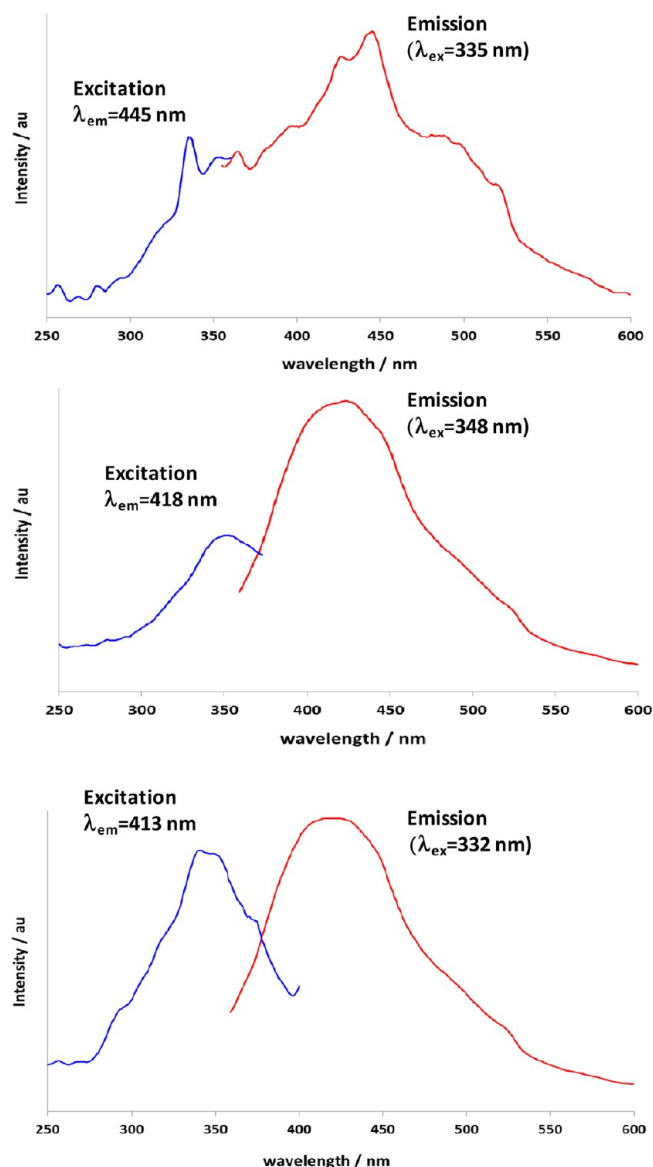


Figure 10. Solid state emission (red) and excitation (blue) spectra of *p*-H₆L (top), **Mg**–(*p*-H₆L) (middle), and **Zn**–(*p*-H₆L) (bottom).

derivative shows no response to UV–vis radiation over the measurable range. All three of the samples that display photoluminescence are excited over the range 332–348 nm, which implies that it is the substituted phenyl ring of the phosphonate anion which is being excited, it is most likely that this arises from a $\pi\text{--}\pi^*$ transition. The emissions of all three are observed with the two metal derivatives are in the range of 413–445 nm with the observed emissions for **Mg**–(*p*-H₆L) and **Zn**–(*p*-H₆L) being seen at 418 and 413 nm, respectively. The two metal based materials also have similar full width at half-maximum (fwhm) values of 105 nm for the Mg derivative and 109 nm for the Zn derivative.

It has been shown elsewhere that ligand to metal charge transfer (LMCT) followed by relaxation of the metal to the

ground state will result in emission at different wavelengths.³⁵ This is not observed for these materials and the similarity of the spectra of the ligand and the metal derived materials therefore suggests that the observed luminescence is entirely ligand based, with the slight change in λ_{max} in the emission spectra being accounted for by formation of the anionic species, which will perturb the electronic structure of the phosphonate to a small extent.

Corrosion Inhibition. Corrosion experiments were designed to explore the ability of ligand *p*-H₈L to act synergistically with metal ions and create a protective film acting as a corrosion barrier on carbon steel surfaces. Two pH regions were included, 2.5 and 5.0, and the overall results are shown in Figure 11.

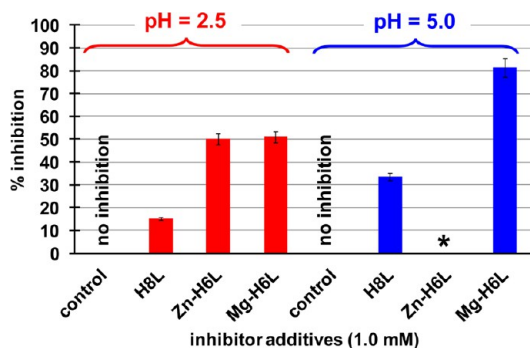


Figure 11. Corrosion inhibition efficiency (%) of the free ligand *p*-H₈L and the hybrids Zn-(*p*-H₆L) and Mg-(*p*-H₆L), compared to the “control” (0% inhibition) at pH 2.5 (red bars) and 5.0 (blue bars). The * indicates that no measurements were made for the Zn-(*p*-H₆L) hybrid due to bulk precipitation.

The *p*-H₈L ligand alone (in the absence of metal ions) offers marginal corrosion protection, with only ~15% efficiency. However, a synergistic combination of Zn²⁺ and *p*-H₈L in a 1:1 molar ratio (under identical conditions used to prepare crystalline Zn-(*p*-H₆L) pH = 2.5) seems to offer increased corrosion protection for carbon steel based on visual observations (Figure 12). According to mass loss measurements, the corrosion rate for the control is 0.138 mm/year whereas that for Zn-(*p*-H₆L) is 0.069 mm/year (~50% inhibition).

A synergistic combination of Mg²⁺ and *p*-H₈L in a 1:1 molar ratio (under identical conditions used to prepare crystalline Mg-(*p*-H₆L), pH = 2.5) seems to offer satisfactory corrosion protection for carbon steel based on visual observations (Figure 13a). According to mass loss measurements the corrosion rate for the control is 0.138 mm/year whereas that for Mg-(*p*-H₆L) is 0.067 mm/year (~51% inhibition), with comparable efficiency to the Zn-(*p*-H₆L) derivative.

An additional set of corrosion testing was carried out at pH 5.0. Corrosion rates are expected to be lower, as the solution pH increases.³⁶ In the presence of ligand *p*-H₈L alone (no metal ions present), the inhibition efficiency is 0.075 mm/year (~34%). For the Mg-(*p*-H₆L) material (at [Mg²⁺]:[H₈L] = 1:1) the results show enhanced efficiency at this pH value, considering that the corrosion rate for the control is 0.113 mm/year, whereas that for Mg-(*p*-H₆L) is 0.021 mm/year (~81%), Figure 13b.

A preliminary set of studies done on the Zn-(*p*-H₆L) anticorrosion film at pH 2.5. EDS showed a Zn:P ratio of ~1:4. The FT-IR spectrum of the film shows a good agreement with

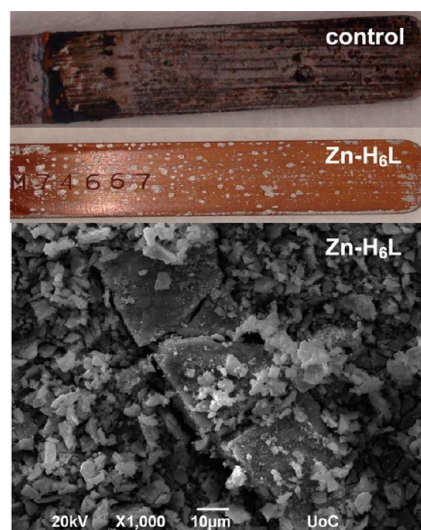


Figure 12. Anticorrosive effect of Zn-(*p*-H₆L) precipitate on carbon steel at pH = 2.2. The upper specimen is the “control” (no inhibitor present). The lower specimen (in the middle) is protected by Zn-(*p*-H₆L) whose SEM is shown as well (at the bottom).

that of an authentic sample of Zn-(*p*-H₆L) (see Supporting Information Figure S17). Finally, the XRD powder patterns of both the Zn-(*p*-H₆L) anticorrosion film at pH 2.5 and Zn-(*p*-H₆L) are essentially identical (Supporting Information Figure S18); however, the film shows poor crystallinity. This is a common phenomenon in metal phosphonate anticorrosion films.^{10,25a,27a,37}

CONCLUSIONS

The principal conclusions derived from this work can be outlined as follows.

- (1) Two families of isostructural hybrids were synthesized at either mild or hydrothermal conditions. These include compounds with the general formula $M[(HO_3PCH_2)_2N(H)CH_2C_6H_4CH_2N(H)(CH_2PO_3H)_2(H_2O)_2] \cdot 2H_2O$ ($M = Mg, Co$ and Zn), $M-(p-H_6L)$, and $M[(HO_3PCH_2)_2N(H)CH_2C_6H_4CH_2N(H)-(CH_2PO_3H)_2] \cdot nH_2O$ ($M = Ca, Mg$, and Zn , $n = 1-1.5$), $M-(m-H_6L)$. Only the cobalt derivative of *m*-H₈L was shown to present polymorphism.
- (2) The basic structural feature of monodimensional $M-(p-H_6L)$ is an organic–inorganic chain, where the phosphonate moiety acts as a bidentate chelating ligand bridging two metal octahedra. $M-(m-H_6L)$ exhibit a 3D pillared open-frameworks with channels containing uncoordinated water, the tetraphosphonate units acting simultaneously as bidentate and monodentate ligand.
- (3) Conductivity values for representative samples of both families of compounds are within the range of other MOF-based water-mediated PCs. Although no significant differences in conductivity were appreciated, the activation energies found points to differences in the mechanism of proton transfer, attributed to variations in hydrogen bond networks for each structural archetype.
- (4) The observed luminescence for derivatives Mg-(*p*-H₆L) and Zn-(*p*-H₆L) is entirely ligand-based, with the slight change in λ_{max} in the emission spectra being accounted for by formation of anionic species, which slightly

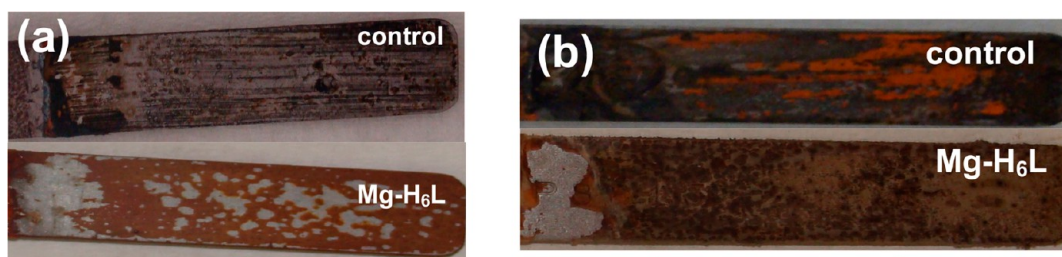


Figure 13. Anticorrosive effect of $\text{Mg}-(p\text{-H}_6\text{L})$ precipitate on carbon steel at (a) pH 2.5 and (b) pH 5.0. The upper specimen is the “control” (no inhibitor present). The lower specimen is protected by $\text{Mg}-(p\text{-H}_6\text{L})$.

perturb the electronic structure of the phosphonate ligand $p\text{-H}_6\text{L}$.

- (5) Combinations of ligand $p\text{-H}_6\text{L}$ and metal ions offer adequate protection to carbon steel surfaces at pH 2.5, with enhanced inhibition efficiency at pH 5.0.

■ ASSOCIATED CONTENT

■ Supporting Information

CIF files for $\text{M}-(p\text{-H}_6\text{L})$ and $\text{M}-(m\text{-H}_6\text{L})$ compounds. Figures S1 and S2: Comparative PXRD patterns for $\text{Co}-(p\text{-H}_6\text{L})$ and $\text{M}-(m\text{-H}_6\text{L})$ compounds. Figures S3 and S4: Rietveld plots for $\text{Mg}-(p\text{-H}_6\text{L})$ and $\text{Zn}-(p\text{-H}_6\text{L})$. Figure S5: Detailed view of the H-bond interactions for $\text{Zn}-(p\text{-H}_6\text{L})$. Figures S6 and S8: Rietveld plots for $\text{Mg}-(m\text{-H}_6\text{L})$ and $\text{Zn}-(m\text{-H}_6\text{L})$ at room temperature, and $\text{Co}-(p\text{-H}_6\text{L})$ at 543 K. Figures S9 and S10: Selected ball and stick and capped stick views for $\text{Co}-(p\text{-H}_6\text{L})$ and $\text{Co}-(m\text{-H}_6\text{L})$. Figure S11: Rietveld plots for $\text{Co}-(m\text{-H}_6\text{L})$ at 573 K. Figures S12 and S13: IR spectra for $\text{M}-(p\text{-H}_6\text{L})$ and $\text{M}-(m\text{-H}_6\text{L})$ compounds. Figure S14: Time dependence of $\log \sigma$ for $\text{Mg}-(p\text{-H}_6\text{L})$ and $\text{Zn}-(m\text{-H}_6\text{L})$ at two RH values. Figures S15 and S16: Complex impedance plane plots for $\text{Mg}-(p\text{-H}_6\text{L})$ and $\text{Zn}-(m\text{-H}_6\text{L})$ at 69% RH. Figure S17: FTIR spectra of the $\text{Zn}-(p\text{-H}_6\text{L})$ anticorrosion film and that of an authentic sample. Figure S18: XRD powder patterns of the $\text{Zn}-(p\text{-H}_6\text{L})$ anticorrosion film and that of an authentic sample. Table S1: Bond length and angles for $\text{M}-(p\text{-H}_6\text{L})$ compounds. Table S2–S4: Selected H-bond interactions for $\text{M}-(p\text{-H}_6\text{L})$ compounds. Table S5 and S6: Selected H-bond interactions for $\text{M}-(m\text{-H}_6\text{L})$ compounds. Table S7: Bond length and angles for $\text{Co}-(p\text{-H}_6\text{L})$ at 473 K. This material is available free of charge via the Internet at <http://pubs.acs.org>.

■ AUTHOR INFORMATION

Corresponding Author

*E-mail addresses: demadis@chemistry.uoc.gr (K.D.D.); aurelio@uma.es (A.C.).

Notes

The authors declare no competing financial interest.

■ ACKNOWLEDGMENTS

The work at UMA was funded by MAT2010-15175 research grant (Spain) which is cofunded by FEDER. The work at the UoC was supported by a grant from the Research Committee of the University of Crete, ELKE (KA 2573). ESRF is thanked for the provision of synchrotron X-ray beamtime at ID31 beamline.

■ REFERENCES

- (1) (a) Special thematic issue on Metal Organic Frameworks. *Chem. Rev.* **2012**, *112*, 673–1268. (b) Special Thematic Issue on Hybrid Materials. *Chem. Soc. Rev.* **2011**, *40*, 453–1152. (c) Themed issue on Coordination chemistry in the solid state. *Dalton Trans.* **2012**, *41*, 3845–4264. (d) Jiang, H.-L.; Xu, Q. *Chem. Commun.* **2011**, *47*, 3351–3370. (e) Meek, S. T.; Greathouse, J. A.; Allendorf, M. D. *Adv. Mater.* **2011**, *23*, 249–267. (f) Themed issue on Metal–Organic Frameworks. *Chem. Soc. Rev.* **2009**, *38*, 1201.
- (2) (a) Functional Metal–Organic Frameworks: Gas Storage, Separation and Catalysis. In *Topics in Current Chemistry*; Schröder, M., Ed.; Springer: New York, 2010; Vol. 293. (b) *Metal organic frameworks: Design and application*; Macgillivray, L. R., Ed.; Wiley: New York, 2010. (c) *Metal–Organic Frameworks. Applications from Catalysis to Gas Storage*; Farrusseng, D., Ed.; Wiley–VCH Verlag & Co. KGaA: Weinheim, Germany, 2011.
- (3) (a) Colodrero, R. M. P.; Papathanasiou, K. E.; Stavgiannoudaki, N.; Olivera-Pastor, P.; Losilla, E. R.; Aranda, M. A. G.; León-Reina, L.; Sanz, J.; Sobrados, I.; Choquesillo-Lazarte, D.; García-Ruiz, J. M.; Atienzar, P.; Rey, F.; Demadis, K. D.; Cabeza, A. *Chem. Mater.* **2012**, *24*, 3780. (b) Bazaga-García, M.; Cabeza, A.; Olivera-Pastor, P.; Santacruz, I.; Colodrero, R. M. P. *J. Phys. Chem. C* **2012**, *116*, 14526–14533. (c) Gómez-Alcántara, M. M.; Cabeza, A.; Olivera-Pastor, P.; Fernández-Moreno, F.; Sobrados, I.; Sanz, J.; Morris, R. E.; Clearfield, A.; Aranda, M. A. G. *Dalton Trans.* **2007**, 2394–2404.
- (4) (a) Taddei, M.; Costantino, F.; Ienco, A.; Comotti, A.; Dau, P. V.; Cohen, S. *Chem. Commun.* **2013**, *49*, 1315–1317. (b) Costantino, F.; Donnadio, A.; Casciola, M. *Inorg. Chem.* **2012**, *51*, 6992–7000. (c) Wharmby, M.; Mowat, M. T.; John, P. S.; Thompson, S. P.; Wright, P. A. *J. Am. Chem. Soc.* **2011**, *133*, 1266–1269. (d) Colodrero, R. M. P.; Cabeza, A.; Olivera-Pastor, P.; Papadaki, M.; Rius, J.; Choquesillo-Lazarte, D.; García-Ruiz, J. M.; Demadis, K. D.; Aranda, M. A. G. *Crys. Growth Des.* **2011**, *11*, 1713–1722. (e) Yang, C.-I.; Song, Y.-T.; Yeh, Y.-J.; Liu, Y.-H.; Tseng, T.-W.; Lu, K.-L. *CrystEngComm* **2011**, *13*, 2678–2686. (f) Attfield, M. P.; Yuan, Z.; Harvey, H. G.; Clegg, W. *Inorg. Chem.* **2010**, *49*, 2656–2666. (g) Taddei, M.; Costantino, F.; Viviani, R. *Inorg. Chem.* **2010**, *49*, 9664–9670. (h) Colodrero, R. M. P.; Cabeza, A.; Olivera-Pastor, P.; Infantes-Molina, A.; Barouda, E.; Demadis, K. D.; Aranda, M. A. G. *Chem.–Eur. J.* **2009**, *15*, 6612–6618.
- (5) *Metal phosphonate chemistry: From synthesis to applications*; Clearfield, A.; Demadis, K. D., Eds.; The Royal Society of Chemistry: London, 2012.
- (6) (a) Yoon, M.; Suh, K.; Natarajan, S.; Kim, K. *Angew. Chem., Int. Ed.* **2013**, *52*, 2688–2700. (b) Liang, X.; Zhang, F.; Feng, W.; Zou, X.; Zhao, C.; Na, H.; Liu, C.; Sun, F.; Zhu, G. *Chem. Sci.* **2013**, *4*, 983–992. (c) Shimizu, G. K. H.; Taylor, J. M.; Dawson, K. W. In *Metal phosphonate chemistry: From synthesis to applications*; Clearfield, A.; Demadis, K. D., Eds.; The Royal Society of Chemistry: London, 2012; Chapter 15, p 493. (d) Jeong, N. C.; Samanta, B.; Lee, C. Y.; Farha, O. K.; Hupp, J. T. *J. Am. Chem. Soc.* **2012**, *134*, 51–54. (e) Colodrero, R. M. P.; Olivera-Pastor, P.; Losilla, E. R.; Aranda, M. A. G.; León-Reina, L.; Papadaki, M.; McKinlay, A. C.; Morris, R. E.; Demadis, K. D.; Cabeza, A. *Dalton Trans.* **2012**, *41*, 4045–4051. (f) Colodrero, R. M. P.; Olivera-Pastor, P.; Losilla, E. R.; Hernández-Alonso, D.; Aranda, M.

- A. G.; León-Reina, R.; Rius, J.; Moreau, B.; Demadis, K. D.; Villemain, D.; Palomino, M.; Rey, F.; Cabeza, A. *Inorg. Chem.* **2012**, *51*, 7689–7698.
- (g) Sadakiyo, M.; Okawa, H.; Shigematsu, A.; Ohba, M.; Yamada, T.; Kitagawa, H. *J. Am. Chem. Soc.* **2012**, *134*, 5472–5475. (h) Sadakiyo, M.; Yamada, T.; Kitagawa, H. *J. Am. Chem. Soc.* **2009**, *131*, 9906–9907. (i) Hurd, J. A.; Vaidhyanathan, R.; Thangadurai, V.; Ratcliffe, C. I.; Moudra-kovski, I. M.; Shimizu, G. K. H. *Nat. Chem.* **2009**, *1*, 705–710. (j) Sahoo, S. C.; Kundu, T.; Banerjee, R. *J. Am. Chem. Soc.* **2011**, *133*, 17950–17958. (k) Shigematsu, A.; Yamada, T.; Kitagawa, H. *J. Am. Chem. Soc.* **2011**, *133*, 2034–2036.
- (7) Kim, S.; Dawson, K. W.; Gelfand, B. S.; Taylor, J. M.; Shimizu, G. K. H. *J. Am. Chem. Soc.* **2013**, *135*, 963–966.
- (8) Ponomareva, V. G.; Kovalenko, K. A.; Chupakhin, A. P.; Dybtsev, D. N.; Shutova, E. S.; Fedin, V. P. *J. Am. Chem. Soc.* **2012**, *134*, 15640–15643.
- (9) (a) Sekine, I.; Shimode, T.; Yuasa, M. *Ind. Eng. Chem. Res.* **1992**, *31*, 434–439. (b) Mosayebi, B.; Kazemeini, M.; Badakhshan, A. *Br. Corr. J.* **2002**, *37*, 217–224. (c) Kouznetsov, Yu. I. *Prot. Met.* **2001**, *37*, 434–439. (d) Balaban-Irmenin, Yu. V.; Rubashov, A. M.; Fokina, N. G. *Prot. Met.* **2006**, *42*, 133–136. (e) Fang, J. L.; Li, Y.; Ye, X. R.; Wang, Z. W.; Liu, Q. *Corrosion* **1993**, *49*, 266–271. (f) Paszternák, A.; Stichleutner, S.; Felhősi, I.; Keresztes, Z.; Nagy, F.; Kuzmann, E.; Vértés, A.; Homonnay, Z.; Pető, G.; Kálmán, E. *Electrochim. Acta* **2007**, *53*, 337–345. (g) Marin-Cruz, J.; Cabrera-Sierra, R.; Pech-Canul, M. A.; Gonzalez, I. *Electrochim. Acta* **2006**, *51*, 1847–1854.
- (10) (a) Demadis, K. D.; Mantzaridis, C.; Raptis, R. G.; Mezei, G. *Inorg. Chem.* **2005**, *44*, 4469–4471. (b) Demadis, K. D.; Katarachia, S. D.; Koutmos, M. *Inorg. Chem. Commun.* **2005**, *8*, 254–258. (c) Demadis, K. D.; Lykoudis, P.; Raptis, R. G.; Mezei, G. *Cryst. Growth Des.* **2006**, *6*, 1064–1067. (d) Demadis, K. D.; Mantzaridis, C.; Lykoudis, P. *Ind. Eng. Chem. Res.* **2006**, *45*, 7795–7800.
- (11) (a) Hix, G. B. In *Metal phosphonate chemistry: From synthesis to applications*; Clearfield, A., Demadis, K. D., Eds.; The Royal Society of Chemistry: London, 2012; Chapter 16, p 525–550. (b) Rocha, J.; Carlos, L. D.; Almeida Paz, F. A.; Ananias, D. *Chem. Soc. Rev.* **2011**, *40*, 926–940. (c) Tang, S.-F.; Pan, X.-B.; Lv, X.-X.; Zhao, X.-B. *J. Solid State Chem.* **2013**, *197*, 139–146. (d) Rao, X. T.; Huang, Q.; Yang, X. L.; Cui, Y. J.; Yang, Y.; Wu, C. D.; Chen, B. L.; Qian, G. D. *J. Mater. Chem.* **2012**, *22*, 3210–3214.
- (12) Angeli, G.; Cabeza, A.; Villemain, D.; Aranda, M. A. G.; Demadis, K. D. Synthesis of Aminomethylene Tetraphosphonic Acids and Their Inorganic-Organic Hybrid Compounds. *Congrès MATERIAUX 2010*; Palais des Congrès de Nantes, France, October 18–22, 2010.
- (13) Villemain, D.; Moreau, B.; Elbilali, A.; Didi, M.-A.; Kaid, M.; Jaffrès, P.-A. *Phosphorus Sulfur Silicon* **2010**, *185*, 2511–2519.
- (14) Colodrero, R. M. P.; Olivera-Pastor, P.; Cabeza, A.; Papadaki, M.; Demadis, K. D.; Aranda, M. A. G. *Inorg. Chem.* **2010**, *49*, 761–768.
- (15) Boulitf, A.; Louer, D. *J. Appl. Crystallogr.* **2004**, *37*, 724–731.
- (16) Altomare, A.; Camalli, M.; Cuocci, C.; Giacobazzi, C.; Moliterni, A.; Rizzi, R. *J. Appl. Crystallogr.* **2009**, *42*, 1197–1202.
- (17) Rietveld, H. M. *J. Appl. Crystallogr.* **1969**, *2*, 65–71.
- (18) Larson, A. C.; Von Dreele, R. B. *General Structure Analysis System (GSAS)*; Los Alamos National Laboratory: Los Alamos, NM, 2004; Report LAUR 86-748.
- (19) Toby, B. H. *J. Appl. Crystallogr.* **2001**, *34*, 210–213.
- (20) winDETA; Novocontrol GmbH: Hundsangen, Germany, 1995.
- (21) NACE Standard TM0169-95 (Item No. 21200), National Association of Corrosion Engineers, Houston TX, U.S.A., 1995; www.nace.org.
- (22) Stock, N.; Stoll, A.; Bein, T. *Microporous Mesoporous Mater.* **2004**, *69*, 65–69.
- (23) (a) Stock, N.; Bein, T. *Angew. Chem., Int. Ed.* **2004**, *43*, 749–752. (b) Stock, N.; Rauscher, M.; Bein, T. *J. Solid State Chem.* **2004**, *177*, 642–647. (c) Zheng, G.-L.; Ma, J.-F.; Yang, J. *J. Chem. Res.* **2004**, 387–388.
- (24) (a) Socrates, G. *Infrared and Raman Characteristic Group Frequencies: Tables and Charts*; John Wiley & Sons: Chichester, 2001. (b) Taddei, M.; Costantino, F.; Vivani, R. *Inorg. Chem.* **2010**, *49*, 9664–9670.
- (25) (a) Demadis, K. D.; Barouda, E.; Raptis, R. G.; Zhao, H. *Inorg. Chem.* **2008**, *48*, 819–821. (b) Barouda, E.; Demadis, K. D.; Freeman, S.; Jones, F.; Ogden, M. I. *Cryst. Growth Des.* **2007**, *7*, 321–327.
- (26) Costantino, F.; Bataille, T.; Audebrand, N.; Fur, E.; Sangregorio, C. *Cryst. Growth Des.* **2007**, *7*, 1881–1888.
- (27) (a) Demadis, K. D.; Barouda, E.; Stavgiannoudaki, N.; Zhao, H. *Cryst. Growth Des.* **2009**, *9*, 1250–1253. (b) Akyol, E.; Öner, M.; Barouda, E.; Demadis, K. D. *Cryst. Growth Des.* **2009**, *9*, 5145–5154.
- (28) Katarachia, S. D.; Demadis, K. D. *Phosphorus Sulfur Silicon* **2004**, *179*, 627–648.
- (29) (a) Taylor, J. M.; Mah, R. K.; Moudrakovski, I. L.; Ratcliffe, C. I.; Vaidhyanathan, R.; Shimizu, G. K. H. *J. Am. Chem. Soc.* **2010**, *132*, 14055–14057. (b) Taylor, J. M.; Dawson, K. W.; Shimizu, G. K. H. *J. Am. Chem. Soc.* **2013**, *135*, 1193–1196.
- (30) Costantino, F.; Donnadio, A.; Casciola, M. *Inorg. Chem.* **2012**, *51*, 6992–7000.
- (31) Colomban, P. *Proton Conductors: Solids, Membranes and Gels Materials and Devices. Chemistry of Solid State Materials*; Cambridge University Press, Cambridge, U.K., 1992; Vol. 2.
- (32) Dippel, T.; Kreuer, K. D. *Solid State Ionics* **1991**, *46*, 3–9.
- (33) Kreuer, K. D. *Solid State Ionics* **2000**, *136*, 149–160.
- (34) Kreuer, K. D.; Weppner, W.; Rabenau, A. *Mater. Res. Bull.* **1982**, *17*, 501–509.
- (35) Singleton, R.; Bye, J.; Dyson, J.; Baker, G.; Ranson, R. M.; Hix, G. B. *Dalton Trans.* **2010**, 39, 6024–6030.
- (36) Demadis, K. D.; Stavgiannoudaki, N. In *Metal phosphonate chemistry: From synthesis to applications*; Clearfield, A.; Demadis, K. D., Eds.; The Royal Society of Chemistry: London, 2012; Chapter 14, p 438–469.
- (37) (a) Demadis, K. D.; Papadaki, M.; Raptis, R. G.; Zhao, H. *J. Solid State Chem.* **2008**, *181*, 679–683. (b) Demadis, K. D.; Papadaki, M.; Raptis, R. G.; Zhao, H. *Chem. Mater.* **2008**, *20*, 4835–4846. (c) Papadaki, M.; Demadis, K. D. *Comments Inorg. Chem.* **2009**, *30*, 89–118. (d) Demadis, K. D.; Papadaki, M.; Varouchas, D. In *Green Corrosion Chemistry and Engineering: Opportunities and Challenges*; Sharma, S. K., Ed.; Wiley-VCH Verlag GmbH & Co., Germany, 2012; Chapter 9, pp 243–296. (e) Demadis, K. D.; Katarachia, S. D.; Koutmos, M. *Inorg. Chem. Commun.* **2005**, *8*, 254–258.

NOTE ADDED IN PROOF

While this paper was in press, an article appeared “High-throughput microwave-assisted discovery of new metal phosphonates”, Feyand, M.; Seidler, C. F.; Deiter, C.; Rothkirch, A.; Lieb, A.; Wark, M.; Stock, N. *Dalton Trans.* **2013**, 42, 8761–8770. The article describes syntheses and structural chemistry of six metal ions (Ca^{2+} , Mn^{2+} , Co^{2+} , Ni^{2+} , Zn^{2+} , and Cd^{2+}) with the ligands $p\text{-H}_8\text{L}$ and $m\text{-H}_8\text{L}$.